Manuscript for CEBAMA benchmark modelling study,
to be submitted July 2019 to journal of Applied Geochemistry, special issue.

Reactive transport modelling of a low-pH concrete / clay interface

Andrés Idiart[1], Marcelo Laviña[1], Georg Kosakowski[2], Benoit Cochepin[3], Johannes C. L. Meeussen[4], Javier Samper[5], Alba Mon[5], Vanessa Montoya[6,7], Isabelle Munier[3], Jenna Poonoosamy[8], Luis Montenegro[5], Guido Deissmann[8], Stephan Rohmen[8], Leonardo Hax Damiani[2], Emilie Coene[1], Acacia Nieves[5]

[1]Amphos 21 Consulting, Barcelona (Spain);

[2]Paul Scherrer Institute, Villigen (Switzerland);

[3]Andra, Châtenay-Malabry (France);

[4]Nuclear Res. and Consultancy Group, Petten (The Netherlands);

[5]Centro de Investigaciones Científicas Avanzadas (CICA), E.T.S. Ingenieros de Caminos, Canales y Puertos, Universidade de A Coruña, A Coruña (Spain);

[6] Department of Environmental Informatics, Helmholtz-Centre for Environmental Research (UFZ), Leipzig (Germany);

[7]Institute for Nuclear Waste Disposal (INE), Karlsruhe Institute of Technology (KIT), Karlsruhe (Germany);

[8]Forschungszentrum Jülich GmbH, IEK-6, Jülich (Germany);

Corresponding author: Andrés Idiart (andres.idiart@amphos21.com)

Abstract

Cement-based materials are key components in the barrier system and structural support of repositories for disposal of nuclear waste. As such, increased understanding of their long-term performance under repository conditions is paramount for the safety assessment. Quantification of the impact that cement-based materials could have on the surrounding barriers and the host rock is essential to assess long-term safety of the repository system. This interaction can impact the physical properties of the system near the interface and needs to be assessed by means of numerical modelling. A reactive transport modelling study of the interaction between a newly-developed low-pH concrete and a clay host rock (i.e. Callovo Oxfordian) over 100 000 years is presented here. The main goal is to build confidence in the consistency of the different modelling approaches and in the application of different reactive transport codes (iCP, ORCHESTRA, OpenGeosys-GEM, CORE^{2D}, and MIN3P) to analyse the performance of the recently developed low-pH concrete within the CEBAMA project. A common setup of a reference case was established, including precipitation/dissolution reactions, redox and cation exchange processes, building upon preliminary cases of increasing complexity. In addition, a set of sensitivity cases was simulated to test the effect of key geochemical and transport parameters on the results, including the impact of porosity changes on the diffusion coefficient and electrochemical couplings. Different reactive transport codes were used in the benchmark. Overall, the results show not only the high level of understanding of the governing processes but also the good agreement obtained with different codes, which is essential to demonstrate the applicability of reactive transport modelling to support safety assessment. The sensitivity and preliminary cases modelled show that the results obtained are much more sensitive to changes to transport parameters and couplings than to the different modelling tools used in each case. In addition, the impact of including or not the slow kinetics of dissolution of the claystone minerals is shown to be negligible in the studied scenarios.

Keywords: Benchmark, reactive transport modelling, low-pH concrete, cement-clay interaction

1 Introduction

Cement-based materials are key components in the multi-barrier system of repositories for disposal of nuclear waste (NEA, 2012). As such, increasing understanding of their long-term evolution is paramount for their performance assessment. Chemical interaction between cement-based materials and the surrounding host rock is one of the most important topics. Indeed, alkaline materials such as concrete, widely used in such disposal, are in chemical disequilibrium when in contact with clay rocks, having a circumneutral pH. This disequilibrium triggers a series of interaction processes driven by mass transport between the two systems. In the long term, the interface between them is subjected to various physico-chemical processes that have an impact on the chemical composition of both systems and, as a result, on their physical (transport and mechanical) properties. These various reactive transport processes develop over large ranges of space and time scales, which are not easily accessible through an experimental approach. Thus, they need to be assessed by means of numerical modelling.

A large body of literature exists dealing with the modelling of cement-clay interactions. Reviews by Gaucher and Blanc (2006), Savage et al. (2007), and Bildstein and Claret (2015) and Savage and Cloet (2018) are comprehensive studies of the level of knowledge and main uncertainties in this field. One of the main open issues is related with the long-term performance of the clay host rock when using recently developed low-pH concretes (e.g. Vehmas et al., 2019c). These materials were developed for different applications, such as limiting the heat of hydration or the pH of the pore solution (e.g. García-Siñeriz et al., 2008). They are based on the use of substantial replacements of cement by supplementary cementitious materials. The Horizon 2020 collaborative project CEBAMA (CEment-BAsed MAterials, properties, evolution, barrier functions) was a research and innovation action granted by the EC in support of the implementation of first-of-the-kind geological repositories for nuclear waste (Altmaier et al., 2017). One of the goals of CEBAMA was to improve the understanding of interaction processes between cementitious and clayey materials (i.e. bentonite, clay rocks). Different approaches were used for modelling and interpretation of experimental data generated within the project and focusing on reactive transport processes that can impact the physical properties of cementitious materials and their interface with clayey systems (Idiart, 2019). Therefore, an integrated modelling study was undertaken to build confidence in the consistency of the different modelling approaches. The work consisted of benchmarking the capabilities of various reactive transport codes to simulate physical and chemical processes governing long-term interactions at a concrete-clay interface.

Many of the previous studies focused on the clayey system, disregarding the alteration of the cementitious barrier (Savage et al., 2002; Gaucher et al., 2004; Watson et al., 2009; Fernández et al., 2010). In those studies, the cementitious system is typically replaced by a fixed concrete water as a boundary condition. Other studies have focused on the prediction of the formation of an alkaline plume (e.g. Soler et al., 2011; Grandia et al., 2010; Sidborn et al., 2014), or the degradation of cementitious systems by clay rock porewaters (Olmeda et al., 2017). More recently, the simultaneous interaction between clayey and cement-based materials has been paid more attention (Trotignon et al., 2006; De Windt et al., 2008; Yang et al., 2008; Marty et al., 2009; Kosakowski and Berner, 2013; Soler, 2013; Liu et al., 2014; Mon et al., 2017; Samper et al, 2018). Marty et al. (2014, 2015) presented a systematic modelling study of the interaction between a Callovo-Oxfordian clay formation and a high-pH concrete. Benchmarking of reactive transport codes in that geochemical system showed a good agreement of model results.

The overall evolution sequence of mineralogical assemblage of concrete made with ordinary Portland cement (OPC; high-pH) during its chemical degradation is well-known (Miller et al., 2000; Marty et al., 2014; Olmeda et al., 2017). However, interactions of low-pH concrete with clayey materials, as studied in this paper, have been given much less attention. Thus, the goal of this study

is not only to build confidence in the modelling approaches by benchmarking reactive transport codes, but mainly to increase the level of understanding of the alteration of low-pH cementitious materials in contact with a clayey system. A reference case was simulated considering a common framework of models and parameters, as well as a set of sensitivity cases for assessing the impact of numerical codes specificities, material variabilities, and uncertainties on the extent of alteration. In this paper, the results and main outcomes obtained with different reactive transport modelling tools are presented and the implications of the study are discussed.

The paper is structured as follows. The conceptual model is described first, together with the parameterization and the numerical implementation into the different reactive transport codes, which are also briefly presented. Then, the results of the reference case obtained with the different reactive transport codes are presented and compared. The main outcomes of the sensitivity analysis are also addressed. Finally, the conclusions of the study are highlighted.

2 Description of studied system

The studied system considers a concrete structure in contact with a clayey host rock at isothermal (25ºC) and fully water saturated conditions. Fickian diffusion is considered as the only solute transport mechanism in the reference case. All aqueous species have the same diffusion coefficient in free solution. A different tortuosity is assumed for each material domain, maintaining electroneutrality of the pore solution (i.e. all solutes have the same effective diffusion coefficient in one given material). Both materials were considered as homogeneous and continuous porous media. It is assumed that no excavation damage zone (EDZ) is present. A one-dimensional setup in Cartesian coordinates is assumed, with a concrete thickness of 0.30 m, in contact with a large mass of claystone with a thickness of 40 m. The geometry and boundary conditions are shown in Fig. 1. Fixed concentration (Dirichlet) at the clay host rock boundary corresponds to the initial porewater composition of the claystone.

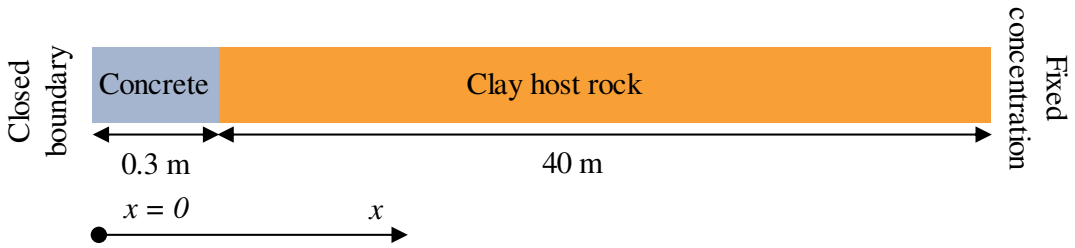

Fig. 1. *Geometry and boundary conditions considered in the model.*

The CEBAMA reference low-pH concrete is considered (Vehmas et al., 2017, 2019c), see Section 2.1 and Appendix A. The mineralogical composition of the clay host rock corresponds to the Callovo-Oxfordian claystone (COx), see Section 2.2, which is well characterised (Marty et al., 2014) and has been previously considered in a benchmark modelling study of the interface between a "high-pH" (OPC) concrete and COx (Marty et al., 2015). The effective diffusion coefficient and total porosity of the two domains are given in Table 1.

Table 1. *Physical properties of the concrete and claystone domains considered in the model.*

Material	**Porosity**	**Pore diffusion coefficient (D_p, m^2/s)**	**Effective diffusion coefficient (D_e, m^2/s)**
Low-pH concrete	0.04	$2.50 \cdot 10^{-11}$	$1.00 \cdot 10^{-12}$
COx claystone	0.18	$1.44 \cdot 10^{-10}$	$2.60 \cdot 10^{-11}$

Most of the simulation cases considered the thermodynamic database ThermoChimie version 9b0 (Giffaut et al., 2014). The main reason to select this database is that it includes consistent data for both, the cementitious and the clayey systems. Data for clay minerals and Portland cement hydrated

phases included in v9b0 were mainly selected from Blanc et al., (2015) and Blanc et al. (2010), respectively. Moreover, the database is under continuous development and regularly updated, so that future cement-clay interaction studies with this database can benefit from the present work. This version of the ThermoChimie database includes parameters for the extended Debye Hückel equation that is used calculate activity coefficients. ORCHESTRA and MIN3P use the Davies equation to calculate activity coefficients, which only requires the ion charges as input.

2.1 Low-pH concrete model

The concrete studied here is made by mixing water with cement, blast furnace slag, silica fume, quartz filler, superplasticizer and aggregates with the proportions specified in Appendix A (Table 9). The composition of the hardened concrete can be calculated by means of thermodynamic modelling, as explained in Appendix A, starting from the raw materials. The initial porosity of the hardened concrete adopted in the reactive transport modelling is 0.04, corresponding to the experimental value obtained by MIP (Table 1). The effective diffusion coefficient of concrete in the reference case is $1 \cdot 10^{-12}$ m^2/s according to Vehmas et al. (2019c) (Table 1). The mineralogical and porewater composition after 10 years of hydration simulated with thermodynamic modelling has been selected as an initial condition (see Appendix A). At that time, the remaining mass of unhydrated clinkers is extremely small and can be neglected, while the slag has dissolved completely. Only silica fume and quartz filler are considered in the simulations to dissolve kinetically with the pH-dependent kinetic dissolution rate of quartz, r (mol/s), proposed by Palandri and Kharaka (2004):

$$r = M_w \cdot m \cdot k \cdot A \cdot \left|1 - \Omega^{\theta}\right|^{\eta} \quad (2.1)$$

$$k = k_{25}^{nu} + \sum_i k_{25}^{i} \prod_j a_{ij}^{n_{ij}} \quad (2.2)$$

where M_w (g/mol) is the molar mass of the mineral, m is the total mass of the mineral (mol), k is the rate constant (mol/m^2/s), A (m^2/g) is the reactive surface area, Ω (-) is the mineral saturation ratio, θ and η are rate parameters (-), superscript *nu* refers to reactions under neutral conditions and superscript i to reactions under either acid or basic conditions, and a_{ij} is the activity of a species *j* in reaction i. The activation energy term is equal to 1 at 25ºC and is thus not included. Table 2 specifies kinetic parameters for quartz filler and silica fume. Surface areas were estimated from the grain size distribution provided by the manufacturers. The aggregates are considered as chemically inert.

The mineralogical and porewater compositions of low-pH concrete are given in Table 3 and Table 4, respectively, corresponding to the results of the hydration model (Appendix A). A volume fraction of inert solid (aggregates and superplasticizer) is also considered in concrete with a value of 0.7748.

In addition, the cementitious system is characterized by surface properties, modelled through cation exchange processes. Table 5 specifies the composition of the cation exchanger in equilibrium with the initial pore solution that simulates the uptake of K and Na (exchanged with Ca) in calcium silicate hydrates (C-S-H). More details are given in Appendix A. The selectivity coefficients are based on the Gaines-Thomas convention. Uptake of aluminium and magnesium in C-S-H is not considered in the model.

The presence of redox sensitive species (i.e. iron, sulphur) in the cementitious system might influence the redox potential of cement porewater, leading to redox potentials in the range -750 mV to -230 mV in OPC (Berner, 2002). That is the case of sulphides in slag blends, and of iron, which can sorb on C-S-H phases, substitutes Al in AFm or AFt phases (e.g. ettringite and monosulfoaluminate, respectively), or precipitate as Ca-ferrites. For low-pH cementitious systems,

no redox potentials are available. With this in mind, and considering that the total dissolved iron concentration does not exceed 10^{-7} M in cement paste (Berner, 2002), a redox potential (Eh) of ~ -27 mV was assumed here by considering a small amount of magnetite (Table 3) and the thermodynamic equilibrium between magnetite and ferrihydrite couple at the given pH.

The secondary minerals allowed to precipitate are listed in Table 3. It is noted that the same set of secondary minerals was considered both in the concrete and COx domains. This includes the potential precipitation of quartz assuming the kinetic law defined for the COx domain (Table 6).

Two potentially relevant groups of phases for the studied system (i.e. low-pH concrete) that are not included in the current version of the thermodynamic database are the group of Magnesium-Silicate-Hydrates (M-S-H phases) and C-(A)-S-H phases. During the course of this work, thermodynamic data for the mentioned phases were reported in Lothenbach et al. (2019) and Roosz et al. (2018). Formation of M-S-H phases at the interface between low-pH concrete and a claystone has been recently identified as one of the relevant alteration processes (e.g. Dauzeres et al., 2016; Mäder et al., 2017). The sink of Mg in the cementitious system is considered by other Mg-bearing phases, namely brucite and hydrotalcite. Due to significantly higher molar volume M-S-H phases compared to other Mg-bearing phases, the impact on porosity could be non-negligible. Partial substitution of Al for Si in C-S-H, so-called C-(A)-S-H phases, is also not accounted for in the model. Instead, strätlingite, an Al-bearing cement hydrate is predicted to form during hydration (Appendix A).

Table 2. *Kinetic parameters for dissolution reactions in concrete (from Palandri and Kharaka, 2004).*

Mineral	A **(m²/g)**	M_w **(g/mol)**	k_{25}^{nu} **(mol/m²s)**	k_{25}^{H+} **(mol/m²s)**	n^{H+}	θ	η
Quartz_filler	0.265	60.08	$3.98107 \cdot 10^{-14}$	$5.12861 \cdot 10^{-17}$	-0.5	1	1
SilicaFume	26.087	64.531	$3.98107 \cdot 10^{-14}$	$5.12861 \cdot 10^{-17}$	-0.5	1	1

Table 3. *Mineralogical composition of low-pH concrete after 10 years of hydration and COx, reaction types, and secondary minerals considered. All reactions considered in thermodynamic equilibrium unless otherwise stated.*

Mineral phases	**mol/L concrete**	**mol/L COx**
CSH 0.8	1.68022	0
Calcite	0.008644	5.038
Ettringite	0.011856	0
Ferrihydrite(am)	0.066384	0
Hydrotalcite	0.046836	0
Magnetite	0.000020	0
Stratlingite	0.047892	0
SilicaFume†	0.496924	-
Quartz filler†	1.748352	-
Quartz*	0	9.1548
Celestite	0	0.1242
Dolomite	0	0.4968
Pyrite	0	0.1908
Siderite	0	0.198
Illite_Imt-2†	0	1.9386
Montmorillonite-BCCa†	0	0.495
Microcline†	0	0.2466
Ripidolite_Cca-2†	0	0.0738
SiO_2(am)	0	0
Brucite	0	0
CSH1.6	0	0
CSH1.2	0	0
C3AH6	0	0
C3FH6	0	0
C4AH13	0	0

C4FH13	0	0
Ettringite-Fe	0	0
Gypsum	0	0
Hemicarboaluminate	0	0
Hydrotalcite-CO_3	0	0
$Fe(OH)_2$(cr)	0	0
Monocarboaluminate	0	0
Monosulfate-Fe	0	0
Monosulfoaluminate	0	0
Portlandite	0	0
Pyrrhotite	0	0
Saponite-FeCa	0	0
Syngenite	0	0
† Dissolution kinetics; * precipitation kinetics		

Table 4. *Initial porewater composition of the low-pH concrete after 10 years of hydration and COx claystone.*

Variable	**Low-pH concrete**	**COx claystone**
pH	10.68	7.06
pe / Eh	-0.46 / -27.2 mV*	-2.84
Totals	**Concentration (mol/kg water)**	**Concentration (mol/kg water)**
Al	$1.448 \cdot 10^{-4}$	$8.504 \cdot 10^{-8}$
C	$1.506 \cdot 10^{-5}$	$3.826 \cdot 10^{-3}$
Ca	$5.237 \cdot 10^{-3}$	$7.601 \cdot 10^{-3}$
Cl	$1.000 \cdot 10^{-10\dagger}$	$4.120 \cdot 10^{-2}$
Fe	$5.447 \cdot 10^{-8}$	$4.351 \cdot 10^{-5}$
K	$3.420 \cdot 10^{-2}$	$5.110 \cdot 10^{-4}$
Mg	$3.736 \cdot 10^{-7}$	$5.187 \cdot 10^{-3}$
Na	$1.910 \cdot 10^{-2}$	$4.008 \cdot 10^{-2}$
S	$3.058 \cdot 10^{-2}$	$1.108 \cdot 10^{-2}$
Si	$2.021 \cdot 10^{-3}$	$1.800 \cdot 10^{-4}$
Sr	$1.000 \cdot 10^{-10\dagger}$	$2.429 \cdot 10^{-4}$
Tracer	$1.000 \cdot 10^{-3}$	0.000

** pe in equilibrium with magnetite/ferrihydrite(am) pair in concrete;*
†Very low value considered in concrete to prevent numerical instabilities when assuming a value of 0.

Table 5. *Initial exchanger compositions for alkali uptake in low-pH concrete and in claystone, and thermodynamic equilibrium constants (Gaines Thomas convention). CEC = cation exchange capacity.*

Concrete	**Log K**	**mol/kg water**	**mol/L concrete**
Ex2Ca	0.0	$4.444 \cdot 10^{-01}$	$1.778 \cdot 10^{-02}$
Ex2K2	0.37	$5.524 \cdot 10^{-01}$	$2.210 \cdot 10^{-02}$
Ex2Na2	0.37	$1.689 \cdot 10^{-01}$	$6.756 \cdot 10^{-03}$
Total (CEC)		2.331	0.093
Claystone	**Log K**	**mol/kg water**	**mol/L COx**
COx2Ca	0.7	$4.744 \cdot 10^{-01}$	$8.540 \cdot 10^{-02}$
COx2Mg	0.7	$3.282 \cdot 10^{-01}$	$5.907 \cdot 10^{-02}$
COxNa	0	$3.867 \cdot 10^{-01}$	$6.961 \cdot 10^{-02}$
COxK	1.2	$7.850 \cdot 10^{-02}$	$1.413 \cdot 10^{-02}$
COx2Sr	0.6	$1.188 \cdot 10^{-02}$	$2.139 \cdot 10^{-03}$
COx2Fe	0.8	$2.860 \cdot 10^{-03}$	$5.145 \cdot 10^{-04}$
Total (CEC)		2.1	0.378

2.2 Claystone model

For the Callovo-Oxfordian claystone (COx), the same physical parameters as in Marty et al. (2015) are used (porosity of 0.18 and effective diffusivity of $2.6 \cdot 10^{-11}$ m^2/s, see Table 1).

The geochemical model of the COx is largely based on the work of Marty et al. (2015), in turn relying on the model by Gaucher et al. (2009). However, the model has been adapted to the ThermoChimie v9b0 database and incorporates two additional cations in the exchanger (Fe^{2+} and Sr^{2+}). The mineralogical composition of the COx is given in Table 3. Most of the minerals are considered under thermodynamic equilibrium, except for five kinetically-controlled minerals (Table 3) based on equations (2-1) and (2-2). Among the kinetically-controlled minerals, only quartz is allowed to precipitate. The kinetic parameters are given in Table 6.

The initial porewater composition (Table 4) is in equilibrium with the cation exchanger composition (Table 5) using thermodynamic equilibrium constants given in the same table (Gaucher et al., 2009).

Table 6. *Kinetic parameters for dissolution reactions in the COx domain (from Marty et al., 2015) and for quartz precipitation.*

Mineral	A **(m²/g)**	k_{25}^{nu} **(mol/m²/s)**	k_{25}^{H+} **(mol/m²/s)**	n^{H+}	k_{25}^{OH-} **(mol/m²/s)**	n^{OH-}	θ	η
Illite_Imt-2	30	$3.3\cdot10^{-17}$	$9.8\cdot10^{-12}$	0.52	$3.1\cdot10^{-12}$	0.38	1	1
Montmorillonite-BCCa	8.5	$9.3\cdot10^{-15}$	$5.3\cdot10^{-11}$	0.69	$2.9\cdot10^{-12}$	0.34	0.17	10.34
Ripidolite_Cca-2	0.003	$6.4\cdot10^{-17}$	$8.2\cdot10^{-09}$	0.28	$6.9\cdot10^{-09}$	0.34	1	1
Microcline	0.11	$1.0\cdot10^{-14}$	$1.7\cdot10^{-11}$	0.27	$1.4\cdot10^{-10}$	0.35	0.09	2.35
Quartz (precipitation)	0.05	$3.0\cdot10^{-12}$	-	-	-	-	4.58	0.54

2.3 Discretization

The same spatial discretization was used in all the 1D models implemented in all the codes. A finer discretization was assumed in the concrete domain and also in the first 0.1 m of the COx domain to avoid using elements of different size at the interface. The size of the elements is 0.02 m in the concrete domain ($0 \leq x \leq 0.30$), while the COx domain ($0.3 < x \leq 40.3$ m) is discretized with the following sequence: 5 x 0.02 m, 35 x 0.04 m, 10 x 0.1 m, 10 x 0.5 m, 10 x 1 m, 10 x 2 m, and 1 x 2.5 m. The total number of elements is 60. This discretization was set as a compromise between spatial resolution and computation time. A simulation time of 100,000 years was considered. According to the von Neumann criterion for diffusive solute transport, the time step size should comply with the following relation:

$$\Delta t < \frac{\Delta x^2}{3 \cdot D_p} \qquad (2\text{-}3)$$

where Δt (s) is the time step size, Δx is the spatial discretization (m), and D_p is the pore diffusivity (m^2/s). Given the higher pore diffusivity of the COx claystone compared to concrete, the time step size is restricted by the clay domain. The temporal discretization considers a constant time step size of 0.10 years. Some of the codes used in this study have an automatic time stepping scheme. In those cases, a maximum time step size of 0.10 years was considered.

2.4 Methodology

Several preliminary cases (P1-P3) of increasing complexity were implemented and simulated step by step in different reactive transport codes (Section 2.5) to finally define the full reference case (FRC). A description of the preliminary cases and the results obtained can be found as Supplementary Material to this paper. In addition, a set of sensitivity cases was modelled with some of the reactive transport codes to assess the impact of some of key parameters and processes (S1-S3). These cases are based on the FRC. Table 7 presents a summary of the main processes considered in each case.

In the sensitivity case S1, the concrete effective diffusion coefficient was reduced 10 times ($1 \cdot 10^{-13}$ m^2/s). This value is closer to the lowest range of experimental results obtained using HTO (Vopálka et al., 2019) and considers the fact that the diffusion coefficient decreases with time with continued hydration (e.g. Vehmas et al., 2019c).

The full reference case does not consider diffusion-porosity coupling, i.e. changes in transport properties (D_e) as a result of porosity variations due to mineral volume changes. Feedback between chemical alteration and porosity and diffusivity was considered in the sensitivity case S2 using a linear relationship between porosity and diffusivity specified by equations (2-4) and (2-5):

$$D_e = D_p \phi \quad (2\text{-}4)$$

$$D_p = \tau D_w \quad (2\text{-}5)$$

with ϕ the porosity (m^3/m^3) and D_p, the pore diffusivity (m^2/s), defined as a function of a constant tortuosity factor (τ) and the diffusion coefficient in free water (D_w in m^2/s). A minimum porosity value of 0.001 is set in the entire modelled domain to prevent full clogging.

Finally, the impact of electrochemical coupling for the transport of charged species was also investigated in sensitivity case S3 and implemented in ORCHESTRA (see Section 2.5). This feature is also available in MIN3P but could not be simulated due to limited resources. This case considered the effects of ion specific diffusion coefficients instead of an average value as in the Fickian diffusion approach. Dissolved species are allowed to diffuse at different rates according to their diffusivities in free solution, which were selected from the phreeqc.dat database (Parkhurst and Appelo, 2013). Due to their different charges, this results in the development of local electric potential gradients. These gradients have an impact on the diffusion rate of charged ions until net charge fluxes are zero. As a result, the diffusion rate of a specific ion not only depends on its own diffusion coefficient, but on the concentration gradients of all accompanying dissolved ions. For this reason, this approach is usually referred to as multicomponent transport and can be modelled using the Nernst-Plank equations (e.g. Galíndez and Molinero, 2010):

$$J_i = -D_i \left(\frac{dc_i}{dx} + z_i c_i \frac{F}{RT} \frac{d\psi}{dx} \right) \quad (2\text{-}6)$$

In equation (2-6), subscript *i* corresponds to variables specific of species *i*, *J* (mol/s) is the diffusive flux, *D* (m^2/s) is the diffusion coefficient, *c* (mol/L) is concentration, *z* is the ion valence, *F* is the Faraday constant (C/mol), *R* (J/K/mol) the constant of ideal gases, *T* is temperature (K), and ψ is the potential (V). During transport, the potential gradient is iteratively solved in ORCHESTRA to result in zero charge flux.

Table 7. *Description of simulation cases and processes considered in this study.*

ID	Description of simulation cases
P1	Preliminary case 1: diffusion of a tracer from concrete into the clay rock
P2	Preliminary case 2: diffusion plus cation exchange and aqueous speciation reactions
P3	Preliminary case 3: idem case P2, and adding mineral reactions in equilibrium
FRC	Full Reference Case: full chemical description of the system, including mineral kinetics
S1	Sensitivity case 1: effective diffusivity of concrete reduced by 1 order of magnitude
S2	Sensitivity case 2: porosity-diffusion coupling considered
S3	Sensitivity case 3: electrochemical coupling (i.e. Nernst-Planck equations)

List of simulated processes	P1	P2	P3	FRC	S1	S2	S3
Tracer diffusion	×	×	×	×	×	×	×
Aqueous species + cation exchange		×	×	×	×	×	×
Minerals in equilibrium			×	×	×	×	×
Reaction kinetics				×	×	×	×
Lower diffusion coefficient in concrete					×		
Porosity-diffusion coupling						×	
Multicomponent diffusion							×

2.5 Description of codes

Five reactive transport codes have been benchmarked: iCP, OpenGeoSys-GEM, ORCHESTRA, ParMIN3P-THCm and CORE^{2D} V5. Their main features are summarized in Table 8 and detailed below.

Table 8. *Relevant features of reactive transport codes used in this study.*

Code name	Spatial discretization	Time stepping scheme	Coupling approach for RT	Chemical equilibrium approach	Aqueous activity coefficient	TDB
iCP	FEM	Pres.	SNIA	LMA	eDH	ThermoChimie
OGS-GEM	FEM	Aut.	SNIA	GEM	eDH	Thermoddem (modified)
ORCHESTRA	FVM	Pres.	SNIA	LMA	Davies	ThermoChimie
CORE^{2D} V5	FEM	Pres.	SIA	LMA	eDH	ThermoChimie
MIN3P	FVM	Aut.	GIA	LMA	Davies	ThermoChimie

FEM: finite element method; FVM: finite volume method; Pres.: prescribed; Aut.: automatic; SNIA: sequential non-iterative approach; SIA: sequential iterative approach; GIA: global implicit approach; LMA: law-of-mass action, GEM, Gibbs energy minimization method; eDH: Extended Debye-Hückel

iCP version 1.5 (interface COMSOL-PHREEQC) couples two standalone codes, the general-purpose software COMSOL Multiphysics® version 5.3 and the geochemical simulator PHREEQC version 3 (Parkhurst and Appelo, 2013). The interface provides a numerical platform to simulate a wide range of multiphysics problems coupled with geochemistry (Nardi et al., 2014). iCP is written in Java and uses the IPhreeqc C^{++} dynamic library and the COMSOL Java-API. The coupling approach is based on the operator-splitting (OS) technique. Conservative solute transport equations coupled with other physical processes are solved by COMSOL, while equilibrium and kinetic chemical reactions are solved by PHREEQC. iCP has been extensively used in geosciences and for long-term performance of engineered barriers for nuclear waste (e.g. Idiart et al., 2019).

OpenGeoSys-GEM (OGS-GEM) is an open-source code for simulation of thermo-hydro-mechanical-chemical processes in porous media that couples the OpenGeoSys V5 framework with the GEMS3K thermodynamic solver (Kosakowski and Watanabe, 2014). It is based on an object-oriented Finite-Element-Method concept (Kolditz et al., 2012). Fluid flow and mass transport equations are solved by OpenGeoSys. The geochemical thermodynamic solver GEMS3K is used

for calculation of local/partial equilibria in complex heterogeneous multicomponent-multiphase systems (Kulik et al., 2013). OpenGeoSys-GEM has been applied extensively to investigate very complex geochemical reactions to assess the long-term geochemical evolution of materials and interfaces in deep geological repositories (Cloet et al., 2018; Kosakowski and Berner, 2013; Kosakowski and Watanabe, 2014; Poonoosamy et al., 2018).

ORCHESTRA (Objects Representing CHEmical equilibrium and TRAnsport) is written in Java (Meeussen, 2003). In ORCHESTRA, all model equations are provided as run-time input, which means that equations can be defined directly in input files in text format. It is also possible to use predefined definitions (objects) from a standard object file (e.g. reactions, minerals, diffusion, etc.). ORCHESTRA has a GUI for defining chemical equilibrium systems, able to read PHREEQC format thermodynamic databases. This makes ORCHESTRA a flexible tool for combining standard chemical / transport models with user defined/modified parts. This approach was followed in the transport modules, where standard objects (e.g. for diffusion) where combined with user defined expressions for feedback between porosity and tortuosity and even for implementing the effect of electric potentials on diffusion (Nernst-Planck). Kinetic reactions were calculated simultaneously with the transport equation, using the same time-step. ORCHESTRA has been used to study solute transport in cement (Sarkar et al., 2010) or cement/clay interaction (Marty et al., 2015).

ParMIN3P-THCm is the parallelized version of MIN3P-THCm, a general-purpose multicomponent reactive transport code to simulate coupled hydrogeological, thermal, and biogeochemical processes in subsurface domains with variable water-saturated conditions (Mayer et al., 2002; Mayer and MacQuarrie, 2010). A hybrid MPI and OpenMP programming approach is implemented in ParMIN3P-THCm with a domain decomposition method based on PETSc libraries (Su et al., 2017).

CORE^{2D} V5 is a code for saturated and unsaturated water flow, heat transport and multicomponent reactive solute transport under both local chemical equilibrium and kinetic conditions in heterogeneous and anisotropic media (Samper et al., 2009; Samper et al., 2011). The flow and transport equations are solved with Galerkin triangular finite elements and an Euler scheme for time discretization, while the chemical formulation is based on ion association theory. CORE^{2D} has been widely used to model laboratory and in situ experiments (Zheng et al., 2011), the interactions of corrosion products and bentonite (Lu et al., 2011) and the long-term geochemical evolution of repositories in granite and clay (Samper et al., 2016; Mon et al., 2017; Samper et al., 2018).

3 Results and discussion

The results of the full reference case (FRC) and 3 sensitivity cases are presented and discussed in this section. Supplementary data is provided separately, including the results of the preliminary simulation cases P1 to P3.

3.1 Full reference case (FRC)

The geochemical evolution of the system of the FRC is presented by means of spatial distribution profiles after 100,000 years of interaction. Comparison of results include porewater composition, exchanger evolution and mineralogical changes of the concrete and claystone domains. The simulations presented in this section were modelled using iCP, ORCHESTRA, MIN3P, OGS-GEM and CORE^{2D}. However, it is noted that the CORE^{2D} model did not consider the minerals under kinetically-controlled precipitation/dissolution. The overall evolution of the system is detailed below.

3.1.1 Porewater evolution

Spatial profiles of aqueous components and solution properties after 100,000 years are presented in Fig. 2 and Fig. 3. Some species present important concentration gradients between concrete and clay porewaters, governed by equilibrium (or kinetic laws) with different sets of minerals and cation distribution in the exchangers. This is the case for Al, C, Mg, Fe, Sr, or Si. Significant Mg and C concentration gradients drive diffusion of these species from the claystone to the concrete, where Mg precipitates as brucite and hydrotalcite (Fig. 6), while calcite formation near the interface is the main sink of C (Fig. 7). In turn, Si diffuses from the concrete to the claystone, coupled to the dissolution of C-S-H (Fig. 6), the formation of quartz (Fig. 7) and the decrease in pH in the degraded concrete region. Ca also diffuses out of the concrete structure throughout the simulation, also driving the dissolution of cement hydrates (C-S-H, ettringite, strätlingite, see Fig. 6).

On the other hand, other species show small variations between concrete and clay due to their null or limited role in solid-liquid interaction, at least after 100,000 years. This is the case for Cl, K, S (mainly as sulfate), or Na. Cl has no interaction with mineral phases or exchanger composition, thus acting as a tracer. Sulphate diffuses out of the concrete domain, triggering ettringite dissolution in concrete and favouring celestite precipitation at both sides of the interface due to the ingress of Sr from the claystone. However, after 100,000 years, the concentration gradient between concrete and claystone has practically vanished. Aluminium concentration decreases in the centre part of the concrete domain due to hydrotalcite precipitation in that region (Fig. 6). Changes in ionic strength of the system are small and agree well between the different codes (Fig. 3).

The pH profile is a suitable indicator of chemical alteration. On the concrete side, pH values after 100,000 years present a maximum value of 10.5 in the innermost 13 cm in concrete, in equilibrium with C-S-H with Ca:Si of 0.8 (Fig. 3). The decrease from the initial value (~10.7) is due to alkali (K) diffusion to the clay. The pH decreases linearly to 10 at x=21 cm and then drops to ~7.3 towards the interface. On the COx side, pH changes are almost negligible, with a value of ~7.3 at the interface decreasing to its initial value towards the right boundary (~7.1). Thus, the maximum increase is predicted at the interface and is equal to ~0.2 pH units.

After 100,000 years, the redox conditions (pe) of COx remain practically unaffected (Eh ~ -170 mV) and controlled by the presence of the accessory minerals pyrite (FeS_2), celestite ($SrSO_4$) and siderite ($FeCO_3$) and the precipitation of small amounts of magnetite (Fe_3O_4) in a reactive front of ~1 m from the interface. Contrarily, an important redox gradient of between -170 mV and 190 mV is established over half of the concrete thickness (0.15 m) mainly due to the pH decrease close to the claystone. This change in pH promotes the dissolution of the iron (III) phase ferrihydrite ($Fe(OH)_3$) and the precipitation/dissolution of the Fe(II)/Fe(III) phase magnetite controlling the Fe(II)/Fe(III) ratio in solution and the redox of concrete. The maximum value of 190 mV at half of the concrete thickness decreases again to its initial value of -30 mV along 7 cm due to changes in the solid phases controlling the pH of the pore solution (i.e. C-S-H gel or hydrotalcite). Finally, weakly reducing conditions (Eh value of -30 mV) are kept constant in the unaltered zone of concrete.

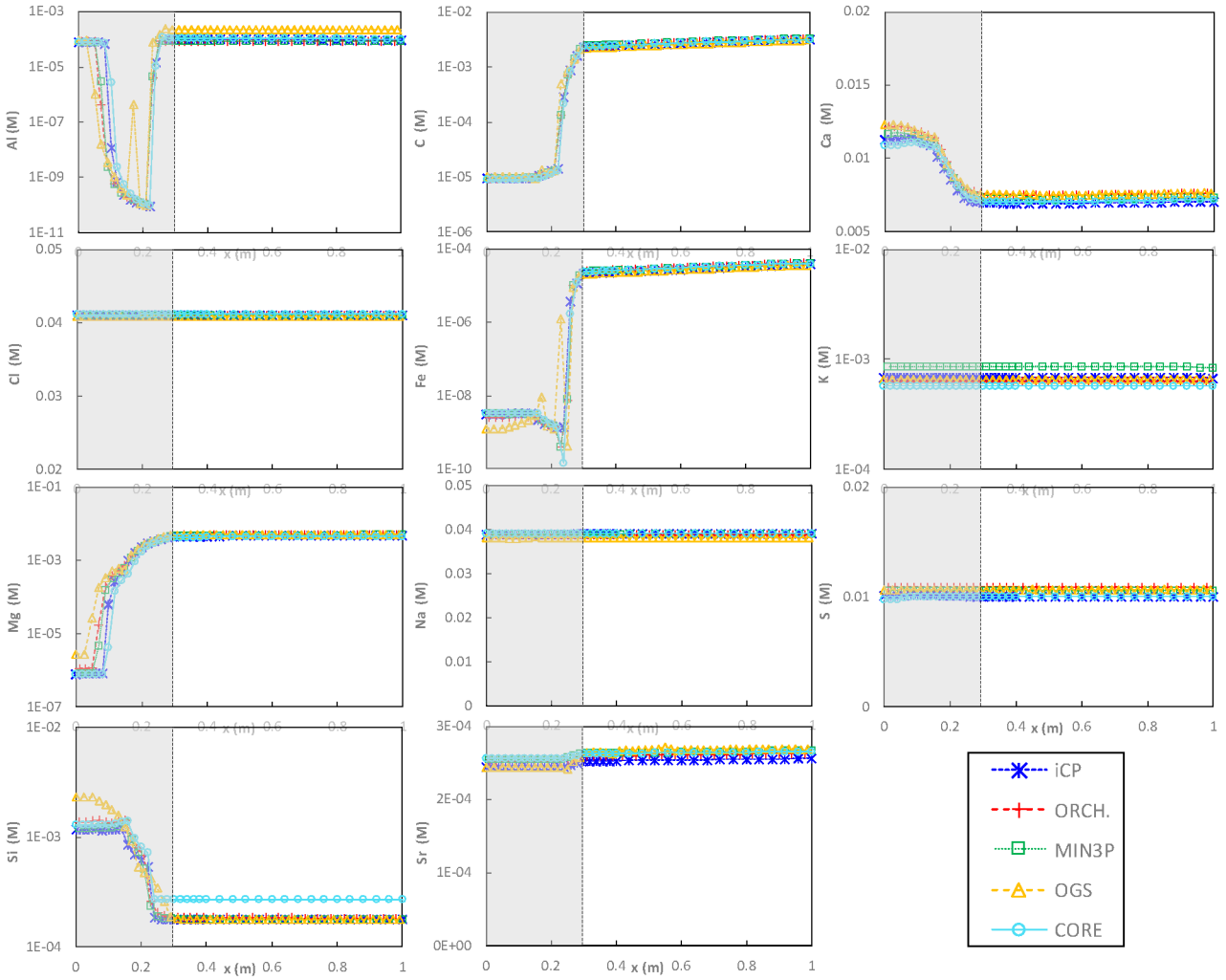

Fig. 2. *Total aqueous species concentration (M) profiles at 100,000 years obtained with iCP, ORCHESTRA, MIN3P, OGS-GEM, and CORE^{2D}.*

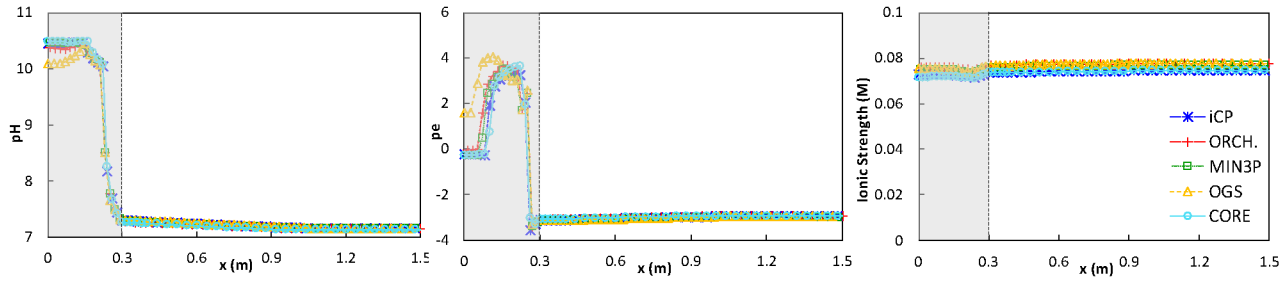

Fig. 3. *pH, pe, and ionic strength profiles at 100,000 years obtained with iCP, ORCHESTRA, MIN3P, OGS-GEM, and CORE^{2D}.*

3.1.2 Cation exchanger composition

The exchanger composition of concrete is shown in Fig. 4. After 100,000 years, K^+ concentration in the concrete exchanger decreases from $5.52 \cdot 10^{-1}$ to ~10^{-4} M due to alkali release to the claystone, resulting in an increase in Na^+ and Ca^{2+} (Fig. 4) with respect to the initial concentrations (Table 5). In the clay, the exchanger at 100,000 years shows a perturbation from the interaction with concrete even far from the interface (Fig. 5). The main cation exchange reaction in the clay is the increase in K^+ from concrete leaching at the expense of a local decrease in Ca^{2+}, Na^+ and Fe^{2+}. In turn, the

concentrations of all other cations show small changes. This is in agreement with the results of Marty et al. (2015) for a high-pH concrete – COx interface.

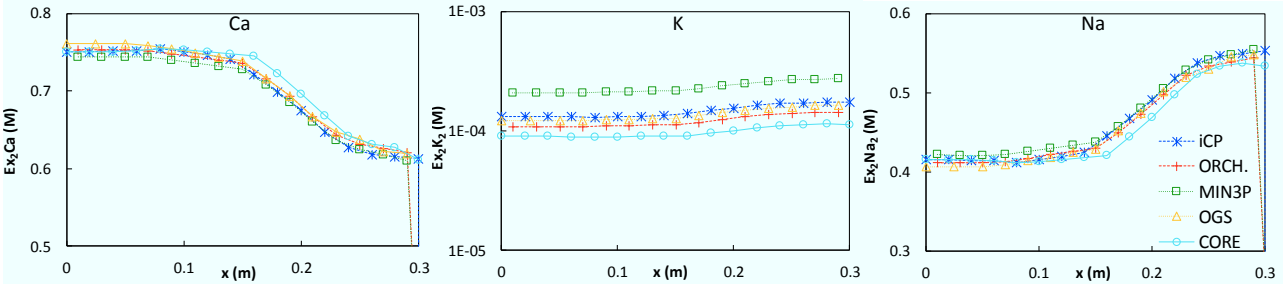

Fig. 4. *Cation concentration (M) profiles in concrete exchanger at 100,000 years obtained with iCP, ORCHESTRA, MIN3P, OGS-GEM, and CORE^{2D}.*

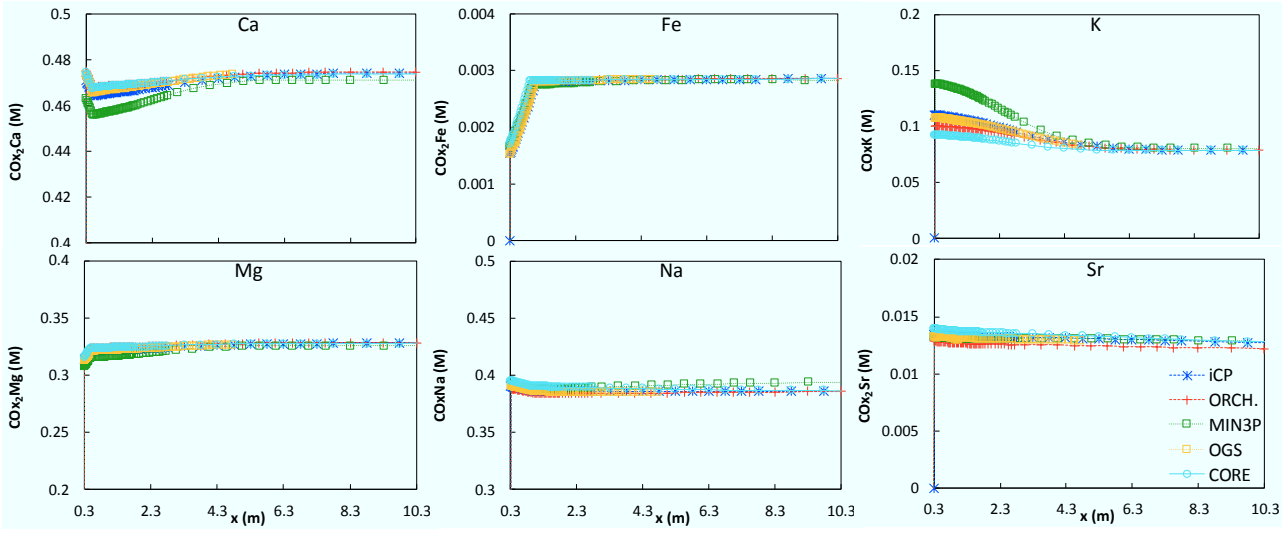

Fig. 5. *Cation concentration (M) profiles in clay exchanger at 100,000 years obtained with iCP, ORCHESTRA, MIN3P, OGS-GEM, and CORE^{2D}.*

3.1.3 Mineralogical changes

Fig. 6 and Fig. 7 present the distribution profiles of mineral phases after 100,000 years of interaction. The mineral degradation sequence is consistent with previous studies (e.g. Gaucher and Blanc, 2006; Savage, 2011; Marty et al., 2015). After 100,000 years, the extent of the alteration front is about 15 cm in concrete (characterized by the complete dissolution of the C-S-H gel) and 20 cm in the claystone. In fact, there are two distinct zones in the COx domain: one strongly altered, whose extension can be characterized by complete dolomite depletion (~20cm), and another one, less disturbed, corresponding to minor mineral alteration, whose extension coincides with that of porosity changes (~50cm, Fig. 7).

This includes dissolution of C-S-H, ettringite, hydrotalcite, strätlingite, and ferrihydrite in concrete with precipitation of brucite and calcite, and reprecipitation of hydrotalcite. In the claystone, the main changes are the dissolution of dolomite and siderite and precipitation of calcite and quartz.

Hydrotalcite and ettringite dissolve completely next to the interface and reprecipitate at the degradation front (Fig. 6). Brucite and Fe-Ca saponite are predicted to form in concrete as secondary phases, while quartz (as a result of C-S-H dissolution and consequent release of Si), magnetite, celestite and calcite precipitate at both sides of the interface. A clear geochemical disturbance is the formation of calcite in concrete and clay close to the interface. Calcite precipitates due to the changes porewater composition: in concrete, due to the ingress of dissolved carbonate

from the COx; in the claystone, due to the diffusion of dissolved calcium and hydroxyl ions from concrete. Calcite is the main phase responsible for porosity clogging in concrete. Quartz filler (Fig. 6) and silica fume (not shown), the two kinetically-controlled mineral phases in concrete, partially dissolve at around x= 23 cm.

Degradation in the claystone is characterized by the dolomite and siderite distribution profiles (Fig. 7). Dolomite is depleted in the first 0.2 m near the interface, and partially dissolves in the next 0.6 m. In turn, siderite completely dissolves in the first 1.1 m, favouring pyrite and magnetite precipitation. Considering the C-S-H gel and dolomite as reference minerals for concrete and COx degradation, respectively, the concrete degradation front extends over half of its thickness (0.15 m), while in the clay the front is at 0.2 m after 100,000 years. Montmorillonite, illite, microcline, and ripidolite concentrations (not shown) remain virtually unchanged after 100,000 years of interaction with the low-pH concrete. This can be explained by their very slow dissolution kinetics at pH < 10.5.

The FRC case does not consider changes in transport properties (porosity and diffusion coefficient) due to mineral volume changes. Thus, no coupling with transport properties or water mass is taken into account. The evolution of porosity in this uncoupled case can still be computed from mineral volume fractions as a post-process of the simulations. These results are presented in Fig. 7. On the concrete side, porosity remains unaltered in the innermost 5 cm. As the degradation front approaches, an increase in porosity is predicted, with values of ~0.10 between x = 0.15 m and x = 0.22 m. However, as geochemical interaction proceeds, porosity decreases mainly due to calcite and brucite precipitation. Negative values are predicted near the interface, showing porosity clogging. On the clay side, porosity decreases over 0.5 m from the interface, although noticeable changes are only predicted for the closest 3 to 7 cm, with values down to 0.12 at the interface.

Overall, the results of the FRC are very similar to case P3 without kinetically-controlled minerals (see Supplementary Material), supporting the comparison of the FRC results of iCP, ORCHESTRA and MIN3P with the P3 results of CORE^{2D}. Including kinetically-controlled mineral phases is, for this particular case, not a key factor. Primary kinetically-controlled minerals in the clay (montmorillonite, illite, microcline and ripidolite) remain unaffected for 100,000 years. In concrete, silica fume and quartz filler are only dissolving locally and are replaced by quartz precipitation. One of the conclusions is that kinetically-controlled minerals do not play an important role in this case.

The results obtained with the different reactive transport codes for mineral concentration profiles are in good agreement, especially for concrete degradation. In the clay domain, dolomite dissolution front agrees well between different codes, while mineral profiles show slight differences when comparing iron-bearing minerals (magnetite, siderite and pyrite).

Some discrepancies between OGS-GEM and other reactive transport codes can be found, especially in the cementitious system. This is due to the following differences in the implementation of this code. First, ThermoChimie database is not available in a version that can be used in Gibbs Energy Minimization method (GEM). Thus, in OGS calculations a modified version of the Thermoddem database (Blanc et al., 2012) was used. However, it was checked that calculated values of Gibbs energy and entropy from both databases typically deviate by less than 10 J/mol. Second, OGS-GEM calculates the liquid phase volume based on volume balance for each cell, even if porosity is not coupled with the diffusion coefficient. In the other codes, a constant liquid phase volume was considered in the FRC. Finally, cation exchange reactions based on Gaines-Thomas convention are used in other codes, while OGS uses an ideal solid-solution implementation based on Vanselov convention.

The results are consistent with previous studies addressing concrete/clay interaction (e.g. Gaucher et al., 2006; Savage et al., 2007; Marty et al., 2014). Recent experimental results obtained within CEBAMA (e.g. Cuevas et al., 2018; González-Santamaría et al., 2019; Mäder et al., 2017; Vhemas

et al., 2019c) also show qualitative agreement, e.g. in the decalcification of concrete, formation of calcite and Mg-rich phases near the interface.

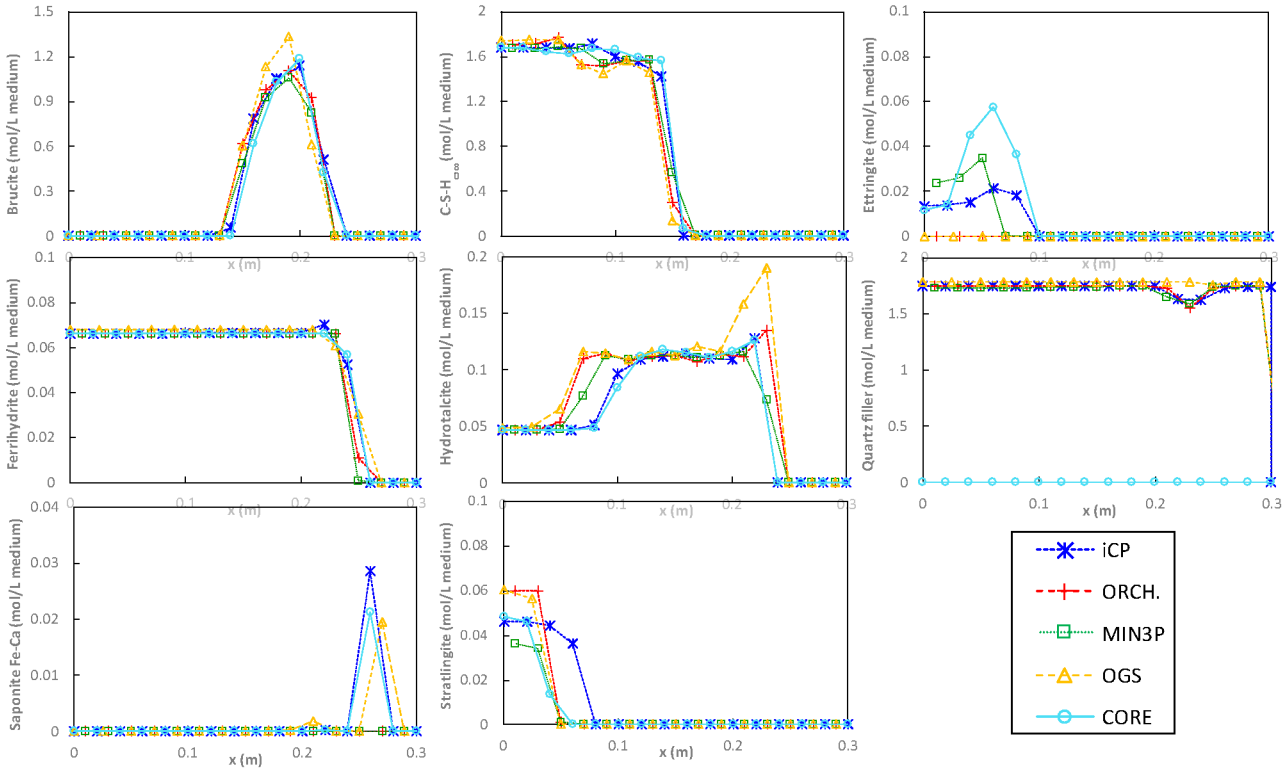

Fig. 6. *Mineral phase profiles (in mol/L medium) in the concrete domain at 100,000 years, obtained with iCP, ORCHESTRA, MIN3P, OGS-GEM, and CORE^{2D}.*

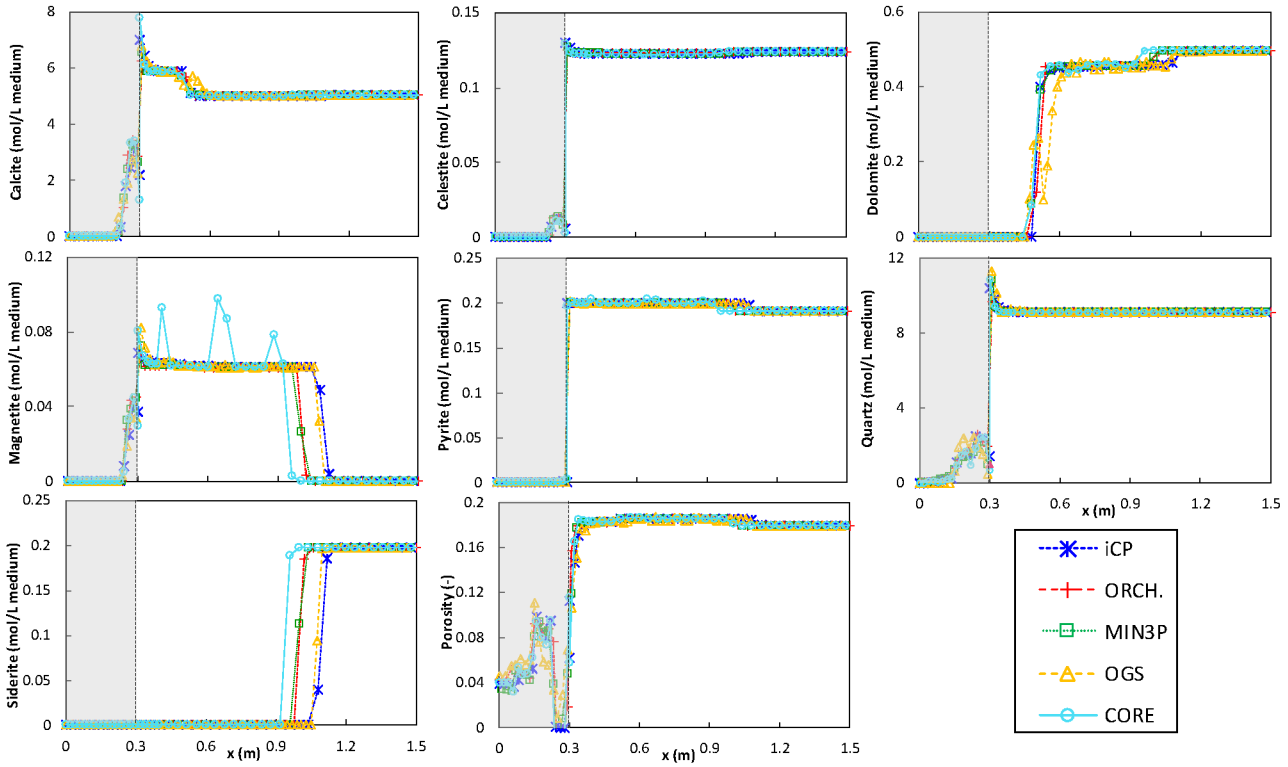

Fig. 7. *Mineral phases (in mol/L medium) and porosity (-) profiles in concrete and clay domains at 100,000 years, obtained with iCP, ORCHESTRA, MIN3P, OGS-GEM, and CORE^{2D}.*

3.2 Reduced concrete diffusion coefficient

A sensitivity case (S1) assuming a lower diffusion coefficient of concrete was simulated with MIN3P, CORE^{2D} and iCP. A constant effective diffusion coefficient of $1 \cdot 10^{-13}$ m^2/s was assumed for the concrete barrier, which is one order of magnitude lower than for the FRC. Fig. 8 shows the porosity, pH and mineralogical distribution profiles at 100,000 years obtained with the three codes. Moreover, the results are compared with the FRC (iCP model results). The results of the three codes for S1 case show a very good agreement. As expected, the level of alteration at a given time is much more limited in this case compared to the FRC due to the reduced concrete diffusivity. Porosity clogging is not predicted to occur even after 100,000 years, and changes are only noticeable over a distance of 0.10 m from the interface. In the concrete domain, pH is lower than 10.5 only close to the interface (4 cm), where C-S-H gel dissolves. This contrasts with the 15 cm degradation front of the FRC. Overall, the degradation sequence is qualitatively consistent with that of the FRC but occurs over a much longer time scale.

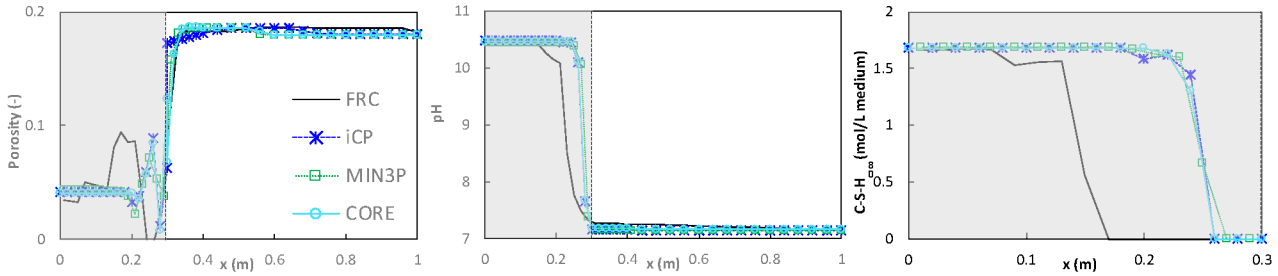

Fig. 8. *Distribution profiles of porosity (-), pH and C-S-H0.8 concentration (mol/L medium) at 100,000 years. Results of iCP, MIN3P and CORE^{2D} for S1 and of FRC (with iCP).*

3.3 Coupling mineral volume changes with transport properties

This sensitivity case (S2) considers the effect of mineral volume changes due to precipitation/dissolution processes on the transport properties, i.e. porosity and diffusion coefficient. This coupling has been previously studied for simple geochemical systems by Xie et al. (2015) and Poonoosamy et al. (2018). The effective diffusion coefficient was chosen to depend linearly on porosity changes, see equations (2-4) and (2-5). Other forms of couplings between porosity and diffusivity were simulated as part of this study and the results can be found in Idiart and Laviña (2019). A minimum porosity value of 0.001 is assumed to avoid complete clogging, corresponding to a minimum effective diffusion coefficient in the low-pH concrete of $2.5 \cdot 10^{-14}$ m^2/s. Four codes were used in this case: iCP, ORCHESTRA, OGS-GEM and CORE^{2D}. MIN3P also includes this porosity coupling feature but could not be used for S2 due to a lack of resources. The differences between these models lie firstly, in the description of mineral reactivity. Kinetically-controlled mineral phases were not included in the CORE^{2D} model. However, as shown for the FRC model setup, only a very small impact is expected due to this simplification. Secondly, the OGS-GEM model considers a fully coupled update of porosity, based on the actual volumetric fluid to solid ratio calculated by the chemical solver.

Fig. 9 presents the results of the four simulations together with the FRC results (iCP model results) for comparison purposes. Two variables are used as indicators of the level of alteration: porosity, which reflects the mineral volume changes, and pH. The mineralogical evolution sequence is similar to the FRC and is not repeated here. Calcite precipitation (not shown) near the interface is the main process responsible for the decrease of porosity to the residual value of 0.001. Porosity clogging is predicted after 50,000 years in iCP and ORCHESTRA (Fig. 9), virtually stopping

further geochemical interaction. Concrete degrades to a less extent compared to the FRC, even before porosity clogging. Porosity decreases at a relatively slower rate in CORE^{2D}, although differences are not significant. The reasons for this discrepancy are still not fully clear.

The temporal porosity changes calculated by OGS-GEM are distinctively different from the other codes, since no porosity clogging is predicted after 100,000 years. This could be due to the inherent difference in the porosity update formulation based on the fluid to solid ratio. As porosity decreases due to mineral precipitation, the volume of reacting fluid also decreases. Thus, the amount of minerals that can precipitate in the next time step also decreases. As a result, the clogging of porosity is delayed. Changes in pH (Fig. 9) are more limited than in the FRC after 100,000 years due to porosity clogging. On the COx domain, pH remains below 7.2 even at the interface. In concrete, dissolution of C-S-H is also more limited in this case, with the degradation front at 5 cm from the interface in iCP and ORCHESTRA. In turn, CORE^{2D} and OGS-GEM results show a much smaller impact compared to the FRC results (Fig. 9), which is due to the relatively lower rate of porosity decrease. The reasons for the lower pH in part of the concrete domain predicted by OGS-GEM are not completely understood but could be related to the description of cation exchange on C-S-H in this code.

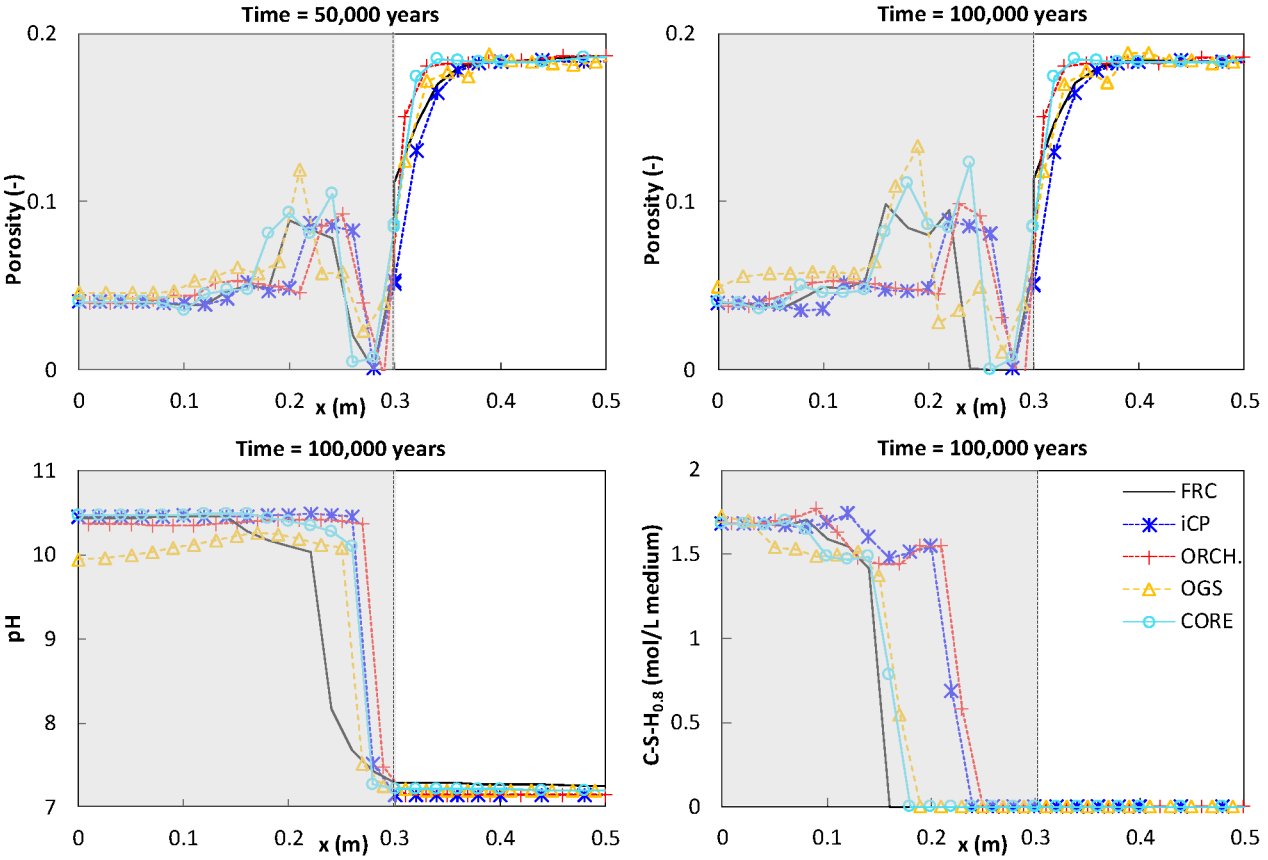

Fig. 9. *Distribution profiles of porosity (-) at 50,000 and 100,000 years, and of pH and C-S-H gel with Ca/Si = 0.8 (in mol/L medium) at 100,000 years. Results for FRC (iCP results) and models coupling porosity with effective diffusion coefficient using iCP, ORCHESTRA, OGS-GEM, and CORE^{2D}.*

3.4 Electrochemical coupling

This sensitivity case (S3) was performed with ORCHESTRA. Multicomponent diffusion can have noticeable impacts in systems containing ions with very different diffusion coefficients. For instance, cementitious systems with hyperalkaline porewater contain large concentrations of OH^-

ions which have a higher diffusion coefficient than other ions. The faster OH^- ions are likely to induce a local potential gradient which in turn affects the diffusion of other ions.

The effect of multicomponent diffusion in the present study can be observed as the development of an electric potential gradient over the cement-clay interface (Fig. 10). The resulting potential difference (ca. 7 mV after 1 year) leads to a reduction of the diffusion rate of OH^- from concrete (and all other accompanying anions) and enhances transport of anions from the claystone towards the concrete. For cations, the potential gradient has the opposite effect. To illustrate this, Fig. 10 shows the enhanced transport from the clay towards concrete of Cl^-, a non-reactive anion in this case, for which the effect of the induced potential gradient on diffusion is most clearly observed when comparing the same simulation with and without the electric potential gradient effect. However, for reactive substances, such as protons (or pH) the effect is much smaller, as shown in Fig. 10. For ions that are in equilibrium with solid phases, concentration gradients are constrained with mineral precipitation/dissolution fronts, so that differences between their aqueous concentrations using both diffusion models are negligible.

The results show furthermore that the electric potential gradient decreases over time because of the lowering of concentration gradients. This implies that the effect of electric potentials on diffusion will also decrease over time, which is illustrated by the small differences between the model results with and without taking into account potential/charge effects. Although the effect of the electrochemical coupling is clearly visible, the impact of the evolving electric potential gradients on the effective ion diffusion rates is probably small in comparison with other uncertainties. Finally, results in terms of porosity distribution show that the effect of the potential gradient on mineral precipitation and dissolution is negligible (Fig. 10), at least after 1,000 years.

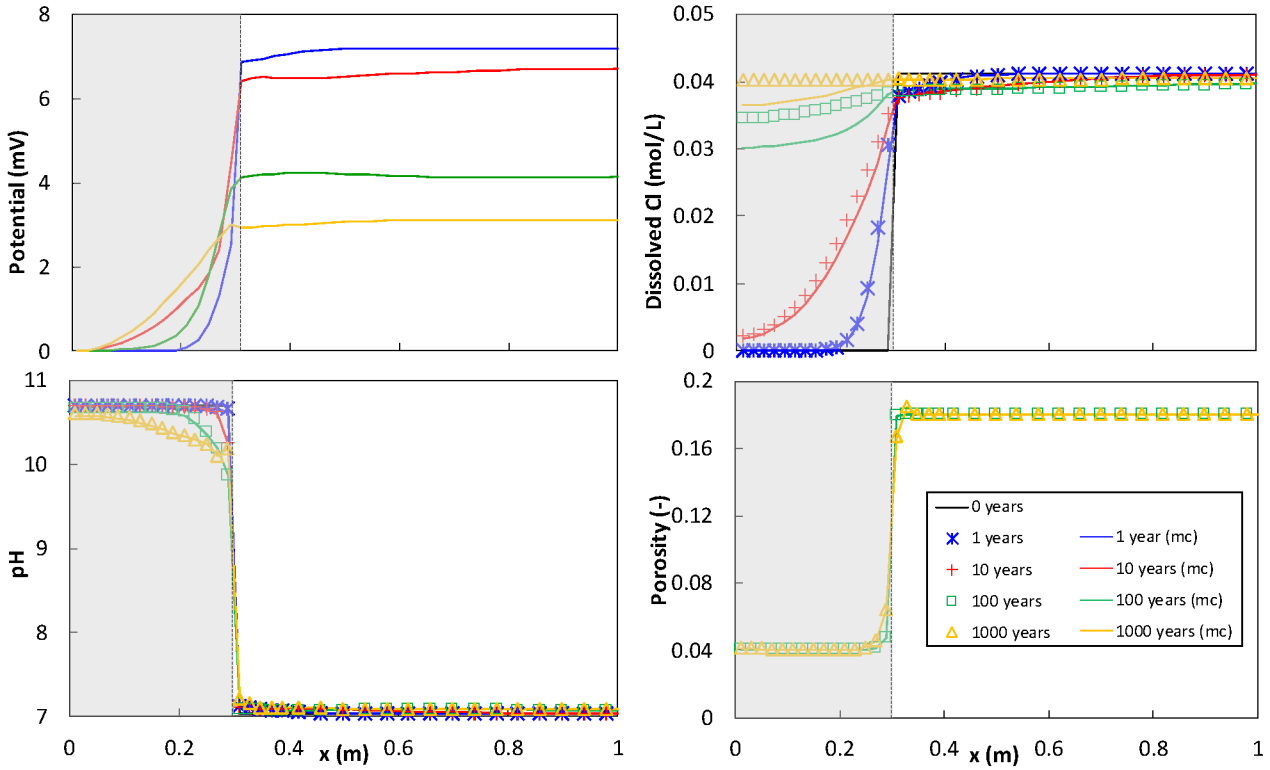

Fig. 10. *Electric potential (mV), dissolved chloride (mol/L), pH, and porosity distribution profiles at 0, 1, 10, 100 and 1,000 years. Results for ORCHESTRA with (mc) and without accounting for potential/charge effects.*

4 Conclusions

The results of the presented modelling study show that different reactive transport codes can be used to quantify the geochemical interaction between a low-pH concrete and a claystone to essentially obtain the same results, despite of inherent differences between modelling approaches. In all modelled cases, the differences observed between models do not have significant consequences on the description of the governing processes and system evolution. This builds confidence in the application of reactive transport codes used within the CEBAMA project to simulate the long-term behaviour of low-pH cementitious systems to be used for disposal of radioactive waste, which is essential for the safety cases (Duro et al., 2019). The impact of key parameters, such as the diffusion coefficient of concrete, electrochemical couplings, and especially the coupling between geochemical and transport parameters, has also been assessed. The impact of including or not the slow kinetics of dissolution of the claystone minerals is shown to be negligible in the studied system. This is in part due to the low-pH nature of the cementitious system, but also to the relatively small concrete volume with respect to the clay rock volume considered in the models. As a general conclusion, the modelling results of sensitivity and preliminary cases show that the system is much more sensitive to changes in the model setup (transport parameters, couplings) than to the different modelling tools used in each case.

A subject for future research concerns the simultaneous modelling of cement hydration with reactive transport processes and water transport at the concrete/clay interface in a partially saturated system. This may be important for concrete mixes with low water-to-binder ratio, as is the case of the studied system. The role of solid solutions to represent cement hydrates, such as C-S-H with lower Ca:Si ratio than 0.8, C-A-S-H, or M-S-H could also be explored. A last issue is the assessment of more realistic couplings between mineral volume changes and their impact on the microstructure and transport properties.

Acknowledgements

The research leading to these results has received funding from the European Union's European Atomic Energy Community's Horizon 2020 Programme (NFRP-2014/2015) under grant agreement, 662147 – CEBAMA. V. Montoya., J. Poonoosamy and G. Deissmann acknowledge the German Federal Ministry of Education and Research (Grant 02NUK053A) and the Initiative and Networking Fund of the Helmholtz Association (Grant SO-093) within the iCross project for partial funding. The authors would like to thank Barbara Lothenbach for fruitful discussions on modelling cement hydration of the low-pH cement system and the two reviewers for constructive and valuable comments that have helped to improve the manuscript.

5 Appendix A – modelling the hydration of low-pH concrete

Characterization of the composition of hardened concrete after curing requires the hydration of the mix to be modelled. The hydrated composition is then used as initial condition in reactive transport models. To model hydration, the methodology developed by Lothenbach and Winnefeld (2006) and Lothenbach et al. (2008) was followed. The model is based on coupling a set of kinetic reactions of dissolution of the mix components with thermodynamic calculations. This Appendix describes the cement hydration model as well as the main results in terms of phase assemblage of the cement hydrates, total porosity, and porewater composition.

Cement hydration modelling was performed with PHREEQC v3 (Parkhurst and Appelo, 2013) using the thermodynamic database ThermoChimie v9b0 (Giffaut et al., 2014), similar to the full reference case. Note that the lowest Ca:Si ratio of the C-S-H model is 0.8. Data of the composition

610 of the raw materials available from CEBAMA (Vehmas et al., 2017, 2019b) and from literature
611 (SKB, 2014) were used as input to the model. The composition of the CEBAMA reference concrete
612 mix is detailed in Table 9. More details can be found in Vehmas et al. (2017, 2019a, 2019c). The
613 stoichiometry of the clinker phases (alite, belite, aluminate, and ferrite), silica fume (SF) and Blast
614 Furnace Slag (BFS) are based on their experimentally-determined oxide composition (Table 10).

615 ***Table 9.*** *Composition of CEBAMA reference concrete mix. Data from Vehmas et al. (2016, 2018, 2019c).*
616 *Density values from material manufacturers.*

Component	**Amount (kg/m^3_{conc})**	**Density (kg/m^3)**	**Volume fraction (-)**
CEM I 42.5	105	3100	0.0339
Silica fume	110	2300	0.0478
Blast furnace slag	65	2900	0.0224
Quartz filler	116	2650	0.0438
Aggregates			
0/1 mm	168	2600	0.0646
0/8 mm	770	2600	0.2962
8/16 mm	532	2600	0.2046
16/32 mm	396	2600	0.1523
Superplasticizer	16.8	1200	0.0140
Water	120	1000	0.1200
Total	2399		0.9996

617

618 ***Table 10.*** *Oxide composition of the components of the CEBAMA reference mix used in the model.*

Oxide	**Mw (g/mol)**	**CEM I[a] (wt. %)**	**SF[b] (wt. %)**	**BFS[c] (wt. %)**
CaO	56.08	64	1.46	41.5
SiO_2	60.08	21	93.1	32.8
Al_2O_3	101.96	3.5	1.44	10.6
SO_3	80.06	2.2	0.47	1.4
MgO	40.30	0.7	0.88	8.29
Fe_2O_3	159.69	4.6	0.91	0.81
K_2O	94.20	0.62	1.73	0.62
Na_2O	61.98	0.07	-	0.62
CO_2	44.01	2.2	-	-
MnO	70.94	-	-	0.42
TiO_2	79.87	-	-	2.04
SrO	103.62	-	-	0.05
V_2O_5	181.88	-	-	0.09
ZrO_2	123.22	-	-	0.03
Total		98.89	99.99	99.27

[a]CEM I 42.5 MH/SR/LA produced by CEMENTA AB (Anläggningscement) (SKB, 2014). [b]SF from Vhemas et al. (2019), [c]BFS measured at VTT (Finland).

619 Cement hydration is assumed to occur under atmospheric conditions at 25°C and 100% relative
620 humidity (i.e. unlimited supply of water for hydration). Redox reactions are not considered in the
621 simulation. Empirical expressions of dissolution rates of clinker phases follow from Parrot and
622 Killoh (1984). The dissolution rate of the BFS is taken from Schöler et al. (2017), while those of SF
623 and quartz filler correspond to that of quartz from Palandri and Kharaka (2004). The latter is based
624 on a pH-dependent transition-state-theory formulation. The specific surface areas of the BFS, SF,
625 and quartz filler are either specified directly by the providers or derived from their particle size

distribution. Apart from these kinetically-controlled reactions, all other chemical reactions are considered under thermodynamic equilibrium. The aggregates and superplasticizer are considered as chemically inert. The alkali uptake in C-S-H phases (Na^+ and K^+) is considered using a cation exchange model based on Missana et al. (2017), with a cation exchange capacity (CEC) that depends on the concentration of C-S-H phases and their Ca/Si ratio (Hong and Glasser, 1999). On the other hand, aluminium and magnesium uptake in C-S-H is not considered in the simulations. Finally, calcium aluminosilicate hydrate (C-A-S-H) or magnesium silicate hydrate (M-S-H) phases are not included in the thermodynamic database.

The dissolution of the clinker, binder components, and quartz filler are shown as a function of time in Fig. 11, together with the precipitation of cement hydrates, in terms of volume fraction (m^3 per m^3 of concrete). An almost complete dissolution of the clinker phases and BFS occurs within the first 100 days. On the other hand, SF rapidly dissolves at the beginning, but after 100 days it slows down significantly. This is due to the drop in pH of the pore solution until reaching a constant value in equilibrium with C-S-H phases that form with a Ca:Si ratio of 0.8. Finally, dissolution of quartz filler is very limited, due to the lower surface area compared to silica fume (see Table 2). The final phase assemblage is composed of unhydrated SF, C-S-H with Ca:Si ratio of 0.8, strätlingite (Al-bearing phase), ettringite (sulphate-bearing phase), and ferrihydrite (Fe-bearing phase). The minerals determined experimentally in the hydrated system are unreacted SF and quartz, C-S-H with a Ca:Si ratio between 0.5 and 0.7, C-A-S-H phases with an Al:Si ratio of 0.05, ettringite, and small amounts of BFS and clinker phases, while absence of portlandite was experimentally confirmed (Vehmas et al., 2019c).

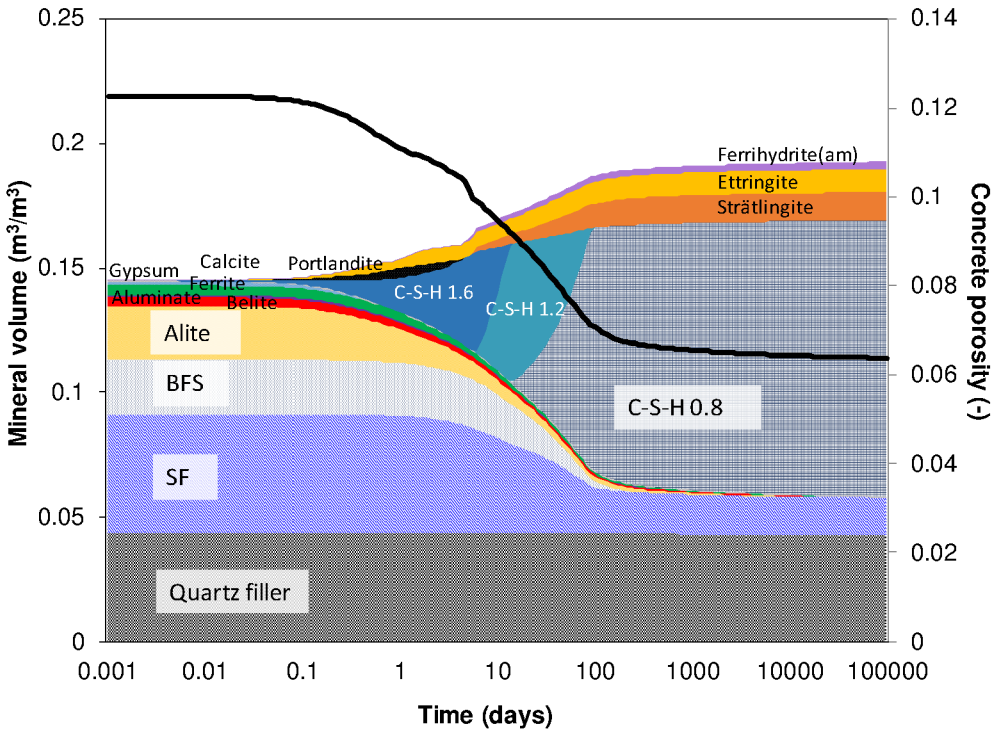

Fig. 11. *Dissolution of the clinker and binder phases, precipitation of main cement hydrates (volume fraction in %) and concrete porosity (-) as a function of hydration time (in days). The black solid line corresponds to porosity.*

The evolution of porewater composition and pH is shown in Fig. 12. The pH of the pore solution fluctuates between 12.5 and 13 at hydration times < 10 days. This short period is followed by large variations in pH until reaching a value of ~10.7 at long hydration times. The evolution of the Ca:Si ratio of the C-S-H has a large impact on the pH of the pore solution as portlandite is already

dissolved after 5 days. The two abrupt changes in pH at 10-12 days and 80-100 days correspond to changes in the Ca:Si ratio of C-S-H, from 1.6 to 1.2, and from 1.2 to 0.8. The values obtained experimentally using the ex-situ leaching method (Alonso et al., 2012) are slightly higher beyond 100 days of hydration, between 11.3 and 11.7 (Vehmas et al., 2019c).

The alkali uptake in the C-S-H phases is also influenced by the pH of the pore solution. Mg^{2+} and Fe^{3+} concentrations in the aqueous solution remain low (< 10^{-6} M) and are controlled by the presence and the low solubility of hydrotalcite and ferrihydrite, respectively. In turn, sulphate concentration remains below $3 \cdot 10^{-2}$ M, controlled by ettringite solubility, while the aluminium concentration is controlled by strätlingite solubility. At pH ≤ 10.7, the dissolution of SF and quartz filler is significantly lowered, and the system virtually reaches equilibrium. In fact, changes observed between hydration times of 10 years, 100 years or 1,000 years are extremely small.

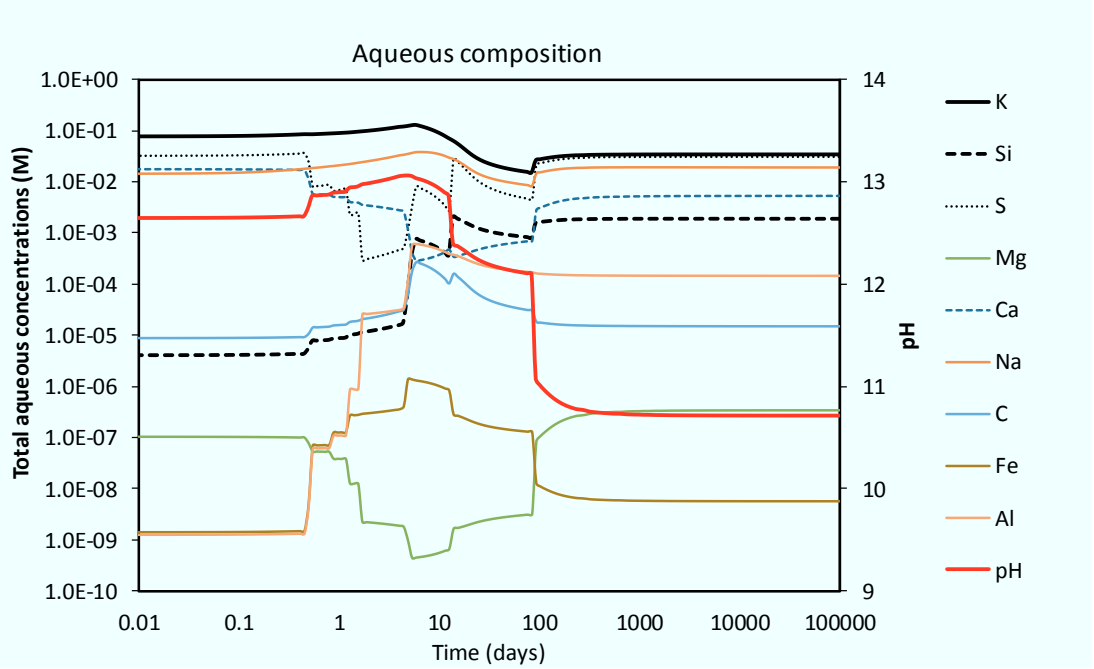

Fig. 12. *Evolution of aqueous composition and pH as a function of hydration time.*

The total porosity, denoted as ϕ_{tot} and calculated with equation (A.1), is shown as a function of hydration time in Fig. 11. The value of total porosity after long hydration times is around 0.063. This value is relatively larger than the value obtained experimentally using mercury intrusion porosimetry (MIP), i.e. 0.038 (Vehmas et al., 2019b, 2019c) and smaller than the values measured with the kerosene method (0.125) or calculated considering the grain density (0.128) (Vehmas et al. 2019c).

$$\phi_{tot} = \frac{V_{b,0}+V_{w,0}-V_{b,t}-V_{hyd,t}}{V_{b,0}+V_{w,0}+V_{aggr}+V_{sp}} \quad \text{(A.1)}$$

In equation (A.1), V stands for volume (litre) and subscripts b, w, hyd, $aggr$, and sp stand respectively for unhydrated binder, water, cement hydrates, aggregates, and superplasticizer (considered inert), respectively, while subscripts 0 and t refer to initial values and values at time t.

6 References

Alonso M. C., Garcia Calvo J. L., Walker C., Naito M., Pettersson S., Puigdomenech I., Cuñado M. A., Vuorio M., Weber H., Ueda H., Fujisaki K. (2012). Development of an accurate pH measurement methodology for the pore fluids of low pH cementitious materials, SKB R-12-02, Svensk Kärnbränslehantering AB.

683 Altmaier M., Montoya V., Duro L., Valls A. (2017). Proc. of the 1st Annual Workshop of the
684 HORIZON 2020 CEBAMA Project. KIT-SR 7734, Karlsruhe, Germany.

685 Berner U. (2002). Project Opalinus Clay: Radionuclide concentration limits in the cementitious
686 near-field of a ILW repository. PSI Bericht 02-26, Switzerland. ISSN 1019-0643.

687 Bildstein O., Claret F. (2015). Stability of clay barriers under chemical perturbations. Chapter 5 -
688 Stability of clay barriers under chemical perturbations, Eds.: C. Tournassat, C. I. Steefel, I. C.
689 Bourg, F. Bergaya, In Developments in Clay Science, Elsevier, Vol. 6, 155-188.
690 https://doi.org/10.1016/B978-0-08-100027-4.00005-X

691 Blanc P., Bourbon X., Lassin A., Gaucher E.C. (2010). Chemical model for cement-based
692 materials: Temperature dependence of thermodynamic functions for nanocrystalline and crystalline
693 C-S-H phases. Cement and Concrete Research, 40, 851-866.
694 https://doi.org/10.1016/j.cemconres.2009.12.004

695 Blanc P., Lassin A., Piantone P., Azaroual M., Jacquemet N., Fabbri A., GaucherE.C. (2012).
696 Thermoddem: A geochemical database focused on low temperature water/rock interactions and
697 waste materials. Appl. Geochem., 27, 2107-2116. https://doi.org/10.1016/j.apgeochem.2012.06.002

698 Blanc P., Vieillard P., Gailhanou H., Gaboreau S., Gaucher E., Fialips C.I., Madé B., Giffaut E.
699 (2015). A generalized model for predicting the thermodynamic properties of clay minerals. Am J
700 Sci, 315, 734-780. https://doi.org/10.2475/08.2015.02

701 Cloet V., Curti E., Kosakowski G., Lura P., Lothenbach B., Wieland, E. (2018). Cementitious
702 backfill for a high-level waste repository: impact of repository induced effects (Nagra
703 Arbeitsbericht NAB 18-05). Nagra, Villigen, Schweiz.

704 Cuevas J., Ruiz A.I., Fernández R., González-Santamaría D., Angulo M., Ortega A., Torres E.,
705 Turrero M.J. (2018). Authigenic Clay Minerals from Interface Reactions of Concrete-Clay
706 Engineered Barriers: A New Perspective on Mg-Clays Formation in Alkaline Environments.
707 Minerals, 8, 362. https://doi.org/10.3390/min8090362

708 Damiani L.H., Kosakowski G., Glaus M.A., Churakov S.V. (2020). A framework for reactive
709 transport modeling using FEniCS-Reaktoro: governing equations and benchmarking results.
710 Computational Geosciences. https://doi.org/10.1007/s10596-019-09919-3

711 Dauzeres A., Achiedo G., Nied D., Bernard E., Alahrache S., Lothenbach B. (2016). Magnesium
712 perturbation in low-pH concretes placed in clayey environment-solid characterizations and
713 modelling. Cement and Concrete Research, 79, 137-150.
714 https://doi.org/10.1016/j.cemconres.2015.09.002

715 De Windt L., Marsal F., Tinseau E., Pellegrini D. (2008). Reactive transport modeling of
716 geochemical interactions at a concrete/argillite interface, Tournemire site (France). Phys. Chem.
717 Earth, 33, S295-S305. https://doi.org/10.1016/j.pce.2008.10.035

718 Duro L., Altmaier M., Holt E., Mäder U., Claret F., Grambow B., Idiart A., Valls A., Montoya V.
719 (2019). Contribution of the results of the CEBAMA project to decrease uncertainties in the Safety
720 Case and Performance Assessment of radioactive waste repositories. Applied Geochemistry,
721 https://doi.org/10.1016/j.apgeochem.2019.104479

722 Fernández R., Cuevas J., Mäder U.K. (2010). Modeling experimental results of diffusion of alkaline
723 solutions through a compacted bentonite barrier. Cem. Concr. Res., 40, 1255-1264.
724 https://doi.org/10.1016/j.cemconres.2009.09.011

725 Galíndez J.M., Molinero J. (2010). On the relevance of electrochemical diffusion for the modeling
726 of degradation of cementitious materials. Cem. Concr. Comp., 32(5), 351-359.
727 https://doi.org/10.1016/j.cemconcomp.2010.02.006

García-Siñeriz J.L., Alonso M.C., Alonso J. (2008). Application of Low pH Concrete in the Construction and the Operation of Underground Repositories. In Proc. of 7th EC Conf. on the Management and Disposal of Radioactive Waste, Euradwaste '08 conference, Luxembourg.

Gaucher E.C., Blanc P. (2006). Cement/clay interactions - a review: experiments, natural analogues, and modeling. Waste Manag., 26(7), 776-788. https://doi.org/10.1016/j.wasman.2006.01.027

Gaucher E.C., Blanc P., Matray J.M., Michau N. (2004). Modeling diffusion of an alkaline plume in a clay barrier. Appl. Geochem., 19, 1505-1515. https://doi.org/10.1016/j.apgeochem.2004.03.007

Gaucher E.C., Tournassat C., Pearson F.J., Blanc P., Crouzet C., Lerouge C., Altmann S. (2009). A robust model for pore-water chemistry of clayrock. Geochim. Cosmochim. Acta, 73(21), 6470-6487. https://doi.org/10.1016/j.gca.2009.07.021

Giffaut E., Grivé M., Blanc P., Vieillard P., Colàs E., Gailhanou H., Gaboreau S., Marty N., Madé B., Duro L. (2014). Andra thermodynamic database for performance assessment: ThermoChimie. Appl. Geochem., 49, 225-236. https://doi.org/10.1016/j.apgeochem.2014.05.007

González-Santamaría D., Angulo M., Ruiz A., Fernández R., Ortega A., Cuevas J. (2018). Low-pH cement mortar-bentonite perturbations in a small-scale pilot laboratory experiment. Clay Minerals, 53(2), 237-254. https://doi.org/10.1180/clm.2018.16

Grandia F., Galíndez J.-M., Molinero J., Arcos D., 2010. Quantitative modelling of the degradation processes of cement grout. Project CEMMOD. SKB TR-10-25. Svensk Kärnbränslehantering AB.

Hong S.-Y., Glasser F.P. (1999). Alkali binding in cement pastes. Part I. The C-S-H phase. Cem. Concr. Res., 29, 1893-1903. https://doi.org/10.1016/S0008-8846(99)00187-8

Idiart A. (editor) 2019. Final results and interpretation of the modelling of experiments within CEBAMA. Deliverable n° D3.06. CEBAMA.

Idiart A., Laviña M. (editors) 2019. Final results and main outcomes of the Modelling Task. Deliverable n° D3.07. CEBAMA.

Idiart A., Olmeda J., Laviña M. (2019). Modelling of concrete degradation in SFL - Influence of concrete mix design. SKB R-19-14. Svensk Kärnbränslehantering AB.

Kolditz O., Bauer S., Bilke L., Böttcher N., Delfs J.O., Fischer T., Görke U.J., Kalbacher T., Kosakowski G., McDermott C.I., Park C.H., Radu F., Rink K., Shao H., Shao H.B., Sun F., Sun Y.Y., Singh A.K., Taron J., Walther M., Wang W., Watanabe N., Wu Y., Xie M., Xu W., Zehner B. (2012). OpenGeoSys: an open-source initiative for numerical simulation of thermo-hydro-mechanical/chemical (THM/C) processes in porous media. Environ. Earth Sci., 67, 589–599. https://doi.org/10.1007/s12665-012-1546-x

Kosakowski G., Berner U. (2013). The evolution of clay rock/cement interfaces in a cementitious repository for low- and intermediate level radioactive waste. Phys. Chem. Earth, Parts A/B/C, 64, 65–86. https://doi.org/10.1016/j.pce.2013.01.003

Kosakowski G., Watanabe N. (2014). OpenGeoSys-Gem: A numerical tool for calculating geochemical and porosity changes in saturated and partially saturated media. Phys. Chem. Earth, Parts A/B/C 70–71, 138–149. https://doi.org/10.1016/j.pce.2013.11.008

Kulik D.A., Wagner T., Dmytrieva S.V., Kosakowski G., Hingerl F.F., Chudnenko K.V., Berner U. (2013). GEM-Selektor geochemical modeling package: revised algorithm and GEMS3K numerical kernel for coupled simulation codes. Computat. Geosci., 17(1), 1-24, https://doi.org/10.1007/s10596-012-9310-6

Liu S., Jacques D., Govaerts J., Wang L. (2014). Conceptual model analysis of interaction at a concrete-Boom Clay interface. Phys. Chem. Earth, 70-71, 150-159. https://doi.org/10.1016/j.pce.2013.11.009

Lothenbach B., Winnefeld F. (2006). Thermodynamic modelling of the hydration of Portland cement. Cem. Concr. Res., 36(2), 209-226. https://doi.org/10.1016/j.cemconres.2005.03.001

Lothenbach B., Matschei T., Möschner G., Glasser F. (2008). Thermodynamic modelling of the effect of temperature on the hydration and porosity of Portland cement. Cem. Conc. Res., 38, 1-18. https://doi.org/10.1016/j.cemconres.2007.08.017

Lothenbach B., Kulik D.A., Matschei T., Balonis M., Baquerizo L., Dilnesa B., Miron D.G., Myers R.J. (2019). Cemdata18: A chemical thermodynamic database for hydrated Portland cements and alkali-activated materials. Cement and Concrete Research, 115, 472-506. https://doi.org/10.1016/j.cemconres.2018.04.018

Lu C., Samper J., Fritz B., Clement A., Montenegro L. (2011) Interactions of corrosion products and bentonite: An extended multicomponent reactive transport model, Phys. Chem. Earth, Parts A/B/C, 36, 1661-1668. https://doi.org/10.1016/j.pce.2011.07.013

Mäder U., Jenni A., Lerouge C., Gaboreau S., Miyoshi S., Kimura Y., Cloet V., Fukaya M., Claret F., Otake T., Shibata M., Lothenbach B. (2017). 5-year chemico-physical evolution of concrete-claystone interfaces. Swiss J. Geosci., 110, 307. https://doi.org/10.1007/s00015-016-0240-5

Marty N.C.M., Tournassat C., Burnol A., Giffaut E., Gaucher E. C. (2009). Influence of reaction kinetics and mesh refinement on the numerical modelling of concrete/clay interactions. J. Hydrol., 364, 58-72. https://doi.org/10.1016/j.jhydrol.2008.10.013

Marty N.C.M., Munier I., Gaucher E., Tournassat C., Gaboreau S., Vong C., Giffaut E., Cochepin B., Claret F. (2014). Simulation of Cement/clay interactions: feedback on the increasing complexity of modelling strategies. Transp. Porous Med., 104(2), 385-405. https://doi.org/10.1007/s11242-014-0340-5

Marty N.C.M., Bildstein O., Blanc P., Claret F., Cochepin B., Gaucher E.C., Jacques D., Lartigue J.E., Liu S., Mayer K.U., Meeussen J.C.L., Munier I., Pointeau I., Su D., Steefel C. (2015). Benchmarks for multicomponent reactive transport across a cement/clay interface. Comput. Geosci., 19(3), 635-653. https://doi.org/10.1007/s10596-014-9463-6

Mayer K.U., Frind E.O., Blowes D.W. (2002). Multicomponent reactive transport modelling in variably saturated porous media using a generalized formulation for kinetically controlled reactions. Water Resour. Res., 38, 1174, https://doi.org/10.1029/2001WR000862

Mayer K.U., MacQuarrie K.T.B. (2010). Solution of the MoMaS reactive transport benchmark with MIN3P - Model formulation and simulation results, Comput. Geosci., 14, 405-419, https://doi.org/10.1007/s10596-009-9158-6

Meeussen J.C.L. (2003). ORCHESTRA: An object-oriented framework for implementing chemical equilibrium models. Environ. Sci. Technol., 37(6), 1175-1182. https://doi.org/10.1021/es025597s

Miller W.M., Alexander W.R., Chapman N.A., McKinley I.G., Smellie J.T. (2000). Geological disposal of radioactive wastes. Pergamon, The Netherlands.

Missana T., García-Gutiérrez M., Mingarro M., Alonso U. (2017). Analysis of barium retention mechanisms on calcium silicate hydrate phases. Cem. Concr. Res., 93, 8-16. https://doi.org/10.1016/j.cemconres.2016.12.004

Mon A., Samper J., Montenegro L., Naves A., Fernández J. (2017). Long-term non-isothermal reactive transport model of compacted bentonite, concrete and corrosion products in a HLW repository in clay. J. Contam. Hydrol., 197, 1-16. https://doi.org/10.1016/j.jconhyd.2016.12.006

Nardi A., Idiart A., Trinchero P., de Vries L.M., Molinero J. (2014). Interface COMSOL-PHREEQC (iCP), an efficient numerical framework for the solution of coupled multiphysics and geochemistry. Comput. & Geosci. 69, 10-21. https://doi.org/10.1016/j.cageo.2014.04.011

NEA (2012). Cementitious Materials in Safety Cases for Geological Repositories for Radioactive Waste: Role, Evolution and Interactions. A Workshop organised by the OECD/NEA Integration Group for the Safety Case and hosted by ONDRAF/NIRAS (NEA-RWM-R-2012-3-REV). Nuclear Energy Agency of the OECD (NEA).

Olmeda J., Henocq P., Giffaut E., Grivé M. (2017). Modelling of chemical degradation of blended cement-based materials by leaching cycles with Callovo-Oxfordian porewater. Phys. Chem. Earth, 99, 110-120. https://doi.org/10.1016/j.pce.2017.05.008

Palandri J.L., Kharaka Y.K. (2004). A Compilation of Rate Parameters of Water-Mineral Interactions Kinetics for Application to Geochemical Modeling. USGS-Report (2004-1068), Menlo Park, California, USA.

Parkhurst D.L., Kipp K.L., Charlton S.R. (2010). PHAST version 2: a program for simulating ground-water flow, solute transport, and multicomponent geochemical reactions. Techniques and Methods 6–A35, USGS, Denver, Colorado.

Parkhurst D.L., Appelo C.A.J. (2013). Description of input and examples for PHREEQC version 3 – A computer program for speciation, batch-reaction, one-dimensional transport, and inverse geochemical calculations, USGS, Denver, Colorado.

Parrot L.J., Killoh D.C. (1984). Prediction of cement hydration, Br. Ceram. Proc., 35, 41-53.

Poonoosamy J., Wanner C., Alt Epping P., Águila J.F., Samper J., Montenegro L., Xie M., Su D., Mayer K.U., Mäder U., Van Loon L.R., Kosakowski G. (2018). Benchmarking of reactive transport codes for 2D simulations with mineral dissolution–precipitation reactions and feedback on transport parameters. Comput. Geosci. https://doi.org/10.1007/s10596-018-9793-x

Roosz C., Vieillard P., Blanc P., Gaboreau S., Gailhanoub H., Braithwaite D., Montouilloute V., Denoyel R., Henocq P., Madé B. (2018) Thermodynamic properties of C-S-H, C-A-S-H and M-S-H phases: Results from direct measurements and predictive modelling. Applied Geochemistry, 92, 140-156. https://doi.org/10.1016/j.apgeochem.2018.03.004

Samper J., Xu T., Yang C. (2009). A sequential partly iterative approach for multicomponent reactive transport with CORE2D. Comput. Geosci., 13, 301-316. https://doi.org/10.1007/s10596-008-9119-5

Samper J., Yang C., Zheng L., Montenegro L., Xu T., Dai Z., Zhang G., Lu C., Moreira S. (2011). CORE^{2D}V4: A code for water flow, heat and solute transport, geochemical reactions, and microbial processes. In: Zhang, F., Yeh, G.-T., Parker, C., Shi, X. (Eds.), Chapter 7 of Groundwater Reactive Transport Models. Bentham Science Publishers. ISBN: 978-1-60805-029 1, pp 161-186.

Samper J., Naves A., Montenegro L., Mon A. (2016). Reactive transport modelling of the long-term interactions of corrosion products and compacted bentonite in a HLW repository in granite: Uncertainties and relevance for performance assessment. Appl. Geochem., 67, 42-51. https://doi.org/10.1016/j.apgeochem.2016.02.001

Samper J., Mon A., Montenegro L., Cuevas J., Turrero M.J., Naves A., Fernández R., Torres E. (2018). Coupled THCM model of a heating and hydration concrete-bentonite column test. Appl. Geochem., 94, 67-81. https://doi.org/10.1016/j.apgeochem.2018.05.007

Sarkar S., Mahadevan S., Meeussen J.C.L., Van der Sloot H., Kosson D.S. (2010). Numerical simulation of cementitious materials degradation under external sulfate attack. Cem. Concr. Compos., 32(3), 241-252. https://doi.org/10.1016/j.cemconcomp.2009.12.005

Savage D., Cloet V. (2018). A review of cement-clay modelling. NAGRA NAB 18-24. National Cooperative for the Disposal of Radioactive Waste.

Savage D., Noy D.J., Mihara M. (2002). Modelling the interaction of bentonite with hyperalkaline fluids. Appl. Geochem., 17, 207-223. https://doi.org/10.1016/S0883-2927(01)00078-6

Savage D., Walker C., Arthur R., Rochelle C., Oda C., Takase H. (2007). Alteration of bentonite by hyperalkaline fluids: a review of the role of secondary minerals. Phys. Chem. Earth, 2, 287-297. https://doi.org/10.1016/j.pce.2005.08.048

Schöler A., Winnefeld F., Ben Haha M., Lothenbach B. (2017). The effect of glass composition on the reactivity of synthetic glasses. J. Am. Ceram. Soc., 100, 2553-2567. https://doi.org/10.1111/jace.14759

Sidborn M., Marsic N., Crawford J., Joyce S., Hartley L., Idiart A., de Vries L. M., Maia F., Molinero J., Svensson U., Vidstrand P., Alexander R. (2014). Potential alkaline conditions for deposition holes of a repository in Forsmark as a consequence of OPC grouting. SKB R-12-17, Svensk Kärnbränslehantering AB.

SKB (2014). Initial state report for the safety assessment SR-PSU. Technical Report SKB TR-14-02. Svensk Kärnbränslehantering AB.

Soler J.M. (2013). Reactive transport modeling of concrete-clay interaction during 15 years at the Tournemire Underground Rock Laboratory. Europ. J. Mineral., 25, 639-654. https://doi.org/10.1127/0935-1221/2013/0025-2324

Soler J.M., Vuorio M., Hautojärvi A. (2011). Reactive transport modeling of the interaction between water and a cementitious grout in a fractured rock. Application to ONKALO (Finland). Appl. Geochem., 26(7), 1115-1129. https://doi.org/10.1016/j.apgeochem.2011.04.001

Su D., Mayer K.U., MacQuarrie K.T.B. (2017). Parallelization of MIN3P-THCm: A high performance computational framework for subsurface flow and reactive transport simulation. Environ. Modell. Softw., 95, 271-289, https://doi.org/10.1016/j.envsoft.2017.06.008

Trotignon L., Peycelon H., Bourbon X. (2006). Comparison of performance of concrete barriers in a clayey geological medium. Phys. Chem. Earth, 31(10–14), 610-617. https://doi.org/10.1016/j.pce.2006.04.011

Vehmas T., Schnidler A., Löija M., Leivo M., Holt E. (2017). Reference mix design and castings for low-pH concrete for nuclear waste repositories. In: Proc. of the 1st Annual Workshop of the HORIZON 2020 CEBAMA Project. KIT-SR 7734, Karlsruhe, Germany.

Vehmas T., Leivo M., Holt E., Alonso M.C, García Calvo J.L., Fernández A., Isaacs M., Rastrick E., Read D., Vašíček R., Hloušek J., Hausmannová L., Večerník P., Červinka R., Havlová V., Lange S., Klinkenberg M., Bosbach D., Deissmann G., Montoya V., Ait Mouheb N., Adam C., Schild D., Schäfer T. (2019a). Cebama reference mix design for low pH concrete and paste, preliminary investigations. In: Proc. 2nd Annual Workshop of CEBAMA Project, 16-19 May 2017, Espoo, Finland. KIT scientific report (in press).

Vehmas T., Leivo M., Holt E., Alonso M.C, Fernández A., García Calvo J.L., Vašíček R., Červinka R., Večerník P., Rosendorf T., Svoboda J., Finck N., Montoya V., Ait Mouheb N., Dardenne K., Rothe J., Schäfer T., Geckeis H., Gaboreau S. (2019b). CEBAMA reference mix design for low-pH concrete and paste, intermediate results. In: Proc. 3rd Annual Workshop of CEBAMA Project, 17-18 April 2018, Nantes, France. KIT scientific report (in press).

902 Vehmas T., Montoya V., Alonso M.C., Vašíček R., Rastrick E., Gaboreau S., Večerník P., Leivo
903 M., Holt E., Ait Mouheb N., Svoboda J., Read D., Červinka R., Vasconcelos R., Corkhill C.
904 (2019c). Characterization Cebama-project Low-pH Reference Concrete and its alteration with
905 representative waters in Radioactive Waste Repositories. (submitted).

906 Vopálka D., Rosendorf T., Štamberg K., Kittnerová J., Baborová L. (2019). Contribution of
907 CTU/UJV to Deliverable D3.06: Final results and interpretation of the modelling of experiments
908 within CEBAMA (Ed. A. Idiart).

909 Watson C., Hane K., Savage D., Benbow S., Cuevas J., Fernández R. (2009). Reaction and
910 diffusion of cementitious water in bentonite: results of 'blind' modelling. Appl. Clay Sci., 45, 54-
911 69. https://doi.org/10.1016/j.clay.2009.03.007

912 Xie M., Mayer K. U., Claret F., Alt-Epping P.,·Jacques D.,·Steefel C.,·Chiaberge C., Simunek J.
913 (2015). Implementation and evaluation of permeability-porosity and tortuosity-porosity
914 relationships linked to mineral dissolution-precipitation. Comput Geosci, 19, 655.
915 https://doi.org/10.1007/s10596-014-9458-3

916 Yang C., Samper J., Montenegro L., 2008. A coupled non-isothermal reactive transport model for
917 long-term geochemical evolution of a HLW repository in clay. Environ. Geol. 53, 1627-1638.
918 https://doi.org/10.1007/s00254-007-0770-2

919 Zheng L., Samper J., Montenegro L. (2011). A coupled THC model of the FEBEX in situ test with
920 bentonite swelling and chemical and thermal osmosis. J. Contam. Hydrol., 126(1-2), 45-60.
921 https://doi.org/10.1016/j.jconhyd.2011.06.003

922

923 7 Supplementary material

924 7.1 Thermodynamic data of minerals

925 ***Table 11.*** *Thermodynamic data from ThermoChimie database (Giffaut et al., 2014) and molar volumes (M_v)*
926 *of minerals (from Thermoddem database, Blanc et al., 2012).*

Mineral phases	M_v (cm^3/mol)	Formula	Log K
CSH 0.8	59.29	$Ca_{0.8}SiO_{2.8}$:1.54H_2O = 0.8Ca^{+2} - 1.6H^+ + 1$H_4(SiO_4)$ + 0.34H_2O	11.05
Calcite	36.93	$CaCO_3$ = 1Ca^{+2} + 1CO_3^{-2}	-8.48
Ettringite	710.32	$Ca_6Al_2(SO_4)_3(OH)_{12}$:26$H_2O$ = 6Ca^{+2} + 2Al^{+3} - 12H^+ + 3SO_4^{-2} + 38H_2O	56.97
Ferrihydrite(am)	34.36	$Fe(OH)_3$ = 1Fe^{+3} - 3H^+ + 3H_2O	2.54
Hydrotalcite	227.36	$Mg_4Al_2(OH)_{14}$:3H_2O = 4Mg^{+2} + 2Al^{+3} - 14H^+ + 17H_2O	73.74
Magnetite	44.52	Fe_3O_4 = 2Fe^{+3} + 1Fe^{+2} - 8H^+ + 4H_2O	10.41
Stratlingite	215.63	$Ca_2Al_2SiO_3(OH)_8$:4H_2O = 2Ca^{+2} + 2Al^{+3} - 10H^+ + 1$H_4(SiO_4)$ + 11H_2O	49.66
SilicaFume	28.06		-
Quartz filler	22.69	SiO_2 = 1$H_4(SiO_4)$ - 2H_2O	-3.74
Quartz	22.69	SiO_2 = 1$H_4(SiO_4)$ - 2H_2O	-3.74
Celestite	46.25	$Sr(SO_4)$ = 1Sr+2 + 1 SO4-2	-6.62
Dolomite	64.3	$CaMg(CO_3)_2$ = 1 Ca^{+2} + 1 Mg^{+2} + 2 CO_3^{-2}	-17.12
Pyrite	23.94	FeS_2 = 1 Fe^{+2} + 2 HS^- - 1 H_2O + 0.5O_2	-58.78
Siderite	29.38	$Fe(CO_3)$ = 1 Fe^{+2} + 1 CO_3^{-2}	-10.80
Illite_Imt-2	139.18	$(Na_{0.044}K_{0.762})(Si_{3.387}Al_{0.613})(Al_{1.427}Fe_{0.292}Fe_{0.084}Mg_{0.241})O_{10}(OH)_2$ = 0.241Mg^{+2} + 0.762K^+ + 0.044Na^+ + 0.292Fe^{+3} + 0.084Fe^{+2} + 2.040Al^{+3} - 8.452H^+ + 3.387$H_4(SiO_4)$ - 1.548H_2O	11.54
Montmorillonite-BCCa	132.48	$Ca_{0.17}Mg_{0.34}Al_{1.66}Si_4O_{10}(OH)_2$ = 0.17Ca^{+2} + 0.34Mg^{+2} + 1.66Al^{+3} - 6 H^+ + 4 $H_4(SiO_4)$ - 4 H_2O	4.20
Microcline	108.74	$KAlSi_3O_8$ = 1 K^+ + 1 Al^{+3} - 4 H^+ + 3 $H_4(SiO_4)$ - 4 H_2O	0.05
Ripidolite_Cca-2	211.92	$(Mg_{2.964}Fe_{1.712}Fe_{0.215}Al_{1.116}Ca_{0.011})(Si_{2.633}Al_{1.367})O_{10}(OH)_8$ = 0.011Ca^{+2} + 2.964Mg^{+2} + 0.215Fe^{+3} + 1.712Fe^{+2} + 2.483Al^{+3} - 17.468H^+ + 2.633$H_4(SiO_4)$ + 7.468H_2O	61.35
SiO_2(am)	29.00	SiO_2 = 1 $H_4(SiO_4)$ - 2 H_2O	-2.71
Brucite	24.63	$Mg(OH)_2$ = 1 Mg^{+2} - 2 H^+ + 2 H_2O	17.10

CSH1.6	84.68	$Ca_{1.6}SiO_{3.6}$:2.58H_2O = 1.6Ca^{+2} - 3.2H^+ + 1 $H_4(SiO_4)$ + 2.18H_2O	28.00
CSH1.2	71.95	$Ca_{1.2}SiO_{3.2}$:2.06H_2O = 1.2Ca^{+2} - 2.4H^+ + 1 $H_4(SiO_4)$ + 1.26H_2O	19.30
C3AH6	149.52	$Ca_3Al_2(OH)_{12}$ = 3 Ca^{+2} + 2 Al^{+3} - 12 H^+ + 12 H_2O	80.32
C3FH6	154.50	$Ca_3Fe_2(OH)_{12}$ = 3 Ca^{+2} + 2 Fe^{+3} - 12 H^+ + 12 H_2O	72.39
C4AH13	269.20	$Ca_4Al_2(OH)_{14}$:6H_2O = 4 Ca^{+2} + 2 Al^{+3} - 14 H^+ + 20 H_2O	103.65
C4FH13	274.4	$Ca_4Fe_2(OH)_{14}$:6H_2O = 4 Ca^{+2} + 2 Fe^{+3} - 14 H^+ + 20 H_2O	95.16
Ettringite-Fe	711.80	$Ca_6Fe_2(SO_4)_3(OH)_{12}$:26$H_2O$ = 6 Ca^{+2} + 2 Fe^{+3} - 12 H^+ + 3 SO_4^{-2} + 38 H_2O	54.55
Gypsum	74.69	$CaSO_4$:2H_2O = 1 Ca^{+2} + 1 SO_4^{-2} + 2 H_2O	-4.61
Hemicarboaluminate	569.02	Ca_6O_6:Al_4O_6:$CaCO_3$:$Ca(OH)_2$:21H_2O = 8 Ca^{+2} + 4 Al^{+3} - 26 H^+ + 1 CO_3^{-2} + 35 H_2O	173.20
Hydrotalcite-CO_3	231.44	$Mg_4Al_2(OH)12CO_3$:2H_2O = 4 Mg^{+2} + 2 Al^{+3} - 12 H^+ + 1 CO_3^{-2} + 14 H_2O	50.86
$Fe(OH)_2$(cr)	24.48	$Fe(OH)_2$ = 1 Fe^{+2} - 2 H^+ + 2 H_2O	12.76
Monocarboaluminate	261.96	$(CaO)_3Al_2O_3$:$CaCO_3$:10.68H_2O = 4 Ca^{+2} + 2 Al^{+3} - 12 H^+ + 1 CO_3^{-2} + 16.68H_2O	70.30
Monosulfate-Fe	316.06	$Ca_4Fe_2(SO_4)(OH)_{12}$:6H_2O = 4 Ca^{+2} + 2 Fe^{+3} - 12 H^+ + 1 SO_4^{-2} + 18 H_2O	66.05
Monosulfoaluminate	311.26	$Ca_4Al_2(SO_4)(OH)_{12}$:6H_2O = 4 Ca^{+2} + 2 Al^{+3} - 12 H^+ + 1 SO_4^{-2} + 18 H_2O	73.07
Portlandite	33.06	$Ca(OH)_2$ = 1 Ca^{+2} - 2 H^+ + 2 H_2O	22.81
Pyrrhotite	18.20	$Fe_{0.87}S$ = 0.87Fe^{+2} - 0.74H^+ + 1 HS^- - 0.13H_2O + 0.065O_2	-11.18
Saponite-FeCa	139.96	$Ca_{0.17}Mg_2FeAl_{0.34}Si_{3.66}O_{10}(OH)_2$ = 0.17Ca^{+2} + 2 Mg^{+2} + 1 Fe^{+2} + 0.34Al^{+3} - 7.36H^+ + 3.66$H_4(SiO_4)$ - 2.64H_2O	26.55
Syngenite	151.63	$K_2Ca(SO_4)_2$:6H_2O = 1 Ca^{+2} + 2 K^+ + 2 $SO4^{-2}$ + 6 H_2O	-7.45

7.2 Description and results of preliminary cases

7.2.1 P1: Tracer diffusion (without considering geochemistry)

Case P1 studied the diffusion of a non-reactive and uncharged tracer from the concrete domain towards the clay host rock in the setup presented in Fig. 1 and Table 1 and the same spatial discretization than the FRC. The initial tracer concentration in the concrete and claystone pore solutions is 1 and 0 mM, respectively (Table 4). A closed boundary condition is imposed on the left and a tracer concentration of 0 on the right. In addition, two alternative reactive transport codes were included in the comparison, namely PHAST (Parkhurst et al., 2010) and NPS (Damiani et al., 2019).

Fig. 13 shows the concentration profiles obtained with several codes at different times. Diffusion of the tracer towards the claystone has the effect of decreasing its concentration in concrete as a function of time. Good comparison between six codes is found for the tracer diffusion. After 100 years, slightly lower concentrations can be found in the concrete domain with MIN3P.

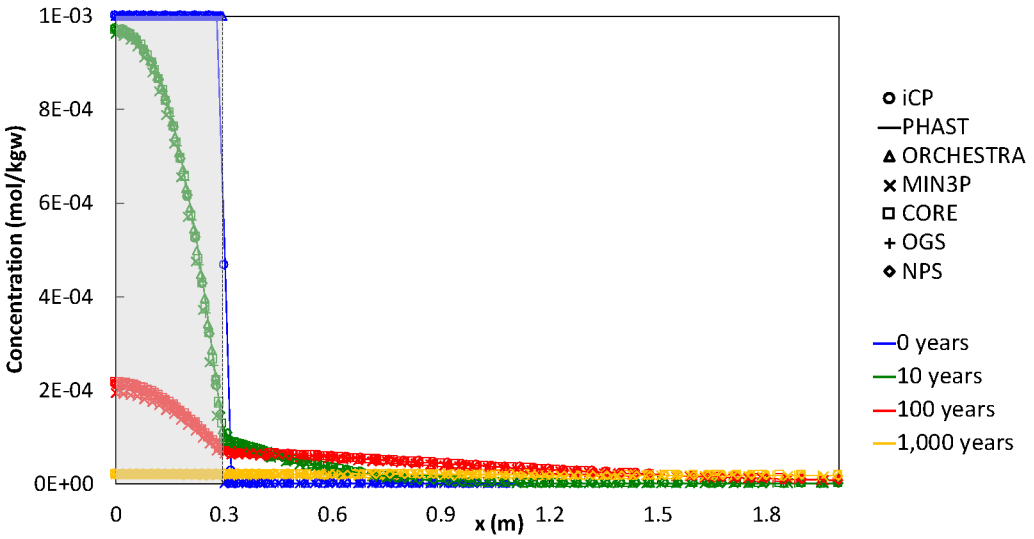

Fig. 13. *Comparison of tracer concentration profiles over 2.1 m (in mol/kg water) at 0, 10, 100 and 1,000 years obtained with iCP, PHAST, ORCHESTRA, CORE^{2D}, MIN3P, OGS-GEM and NPS.*

7.2.2 P2: Aqueous species and cation exchange

Case P2 is equivalent to the FRC but without any primary or secondary minerals, i.e. only the aqueous solutions and cation exchange reactions are considered. The goal was to benchmark the implementation of cation exchange reactions before implementing mineral reactions. Concrete/clay interaction is thus limited to porewater diffusion and cation exchange in thermodynamic equilibrium. This case was simulated with iCP, MIN3P, OGS-GEM and CORE^{2D}. Results after 1,000 years of interaction centred on the first meter of the studied system are presented from Fig. 14 to Fig. 16. Concrete exchanger concentrations of Ca^{2+}, K^+ and Na^+ at 1,000 years (Fig. 14). K^+ release (initial concentration of 0.55 mol/L) to concrete porewater driven by diffusion towards the claystone is the main process. This decrease in K^+ fraction in the exchanger is compensated by an increase in Na^+ (initial concentration of 0.17 mol/L), diffusing from the claystone, and in Ca^{2+}. Ca^{2+} concentration remains unchanged at x = 0 (initial concentration of 0.45 mol/L). Na^+ and Ca^{2+} concentrations changes in the exchanger maintain a similar Ca/Na ratio in the concrete exchanger. Overall, good agreement between codes is found, with slight differences in the results of MIN3P. In turn, Fig. 15 shows the composition of the exchanger within the first meter of claystone. Potassium diffusion from concrete results in an important concentration increase in the clay exchanger. As a consequence, all other cation concentrations are reduced.

Total dissolved calcium and potassium distribution profiles at 1,000 years show the in-diffusion into concrete of the former from the clay and the out-diffusion of the latter (Fig. 16). After 1,000 years, only small variations are observed in the pH profile (Fig. 16), with values between 7.1 and 7.2 for the two materials (initial pH is 10.68 and 7.06 for concrete and clay, respectively). As the clayey domain has a much larger volume (~130 times) than the concrete one, pH tends to the clay initial values in the system. Differences in porewater between codes can be directly linked with the differences observed in the exchanger compositions.

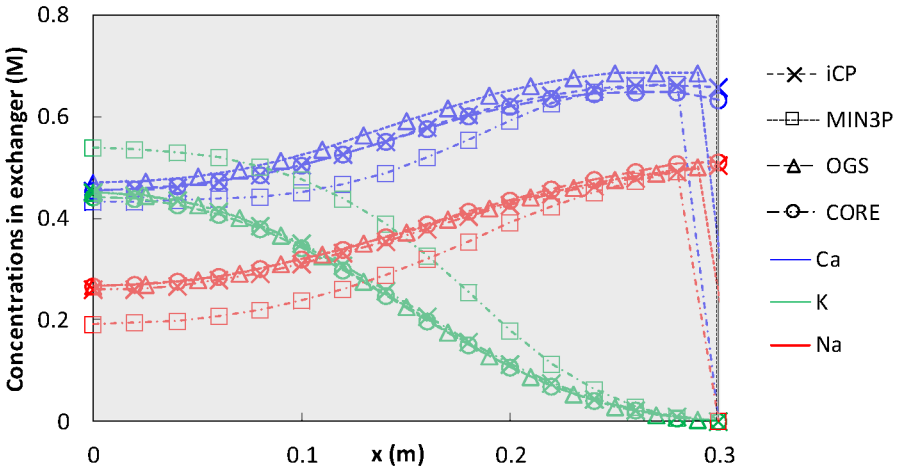

Fig. 14. *Cation concentration (M) profiles in concrete exchanger at 1,000 years obtained with iCP, MIN3P, OGS-GEM and CORE^{2D}.*

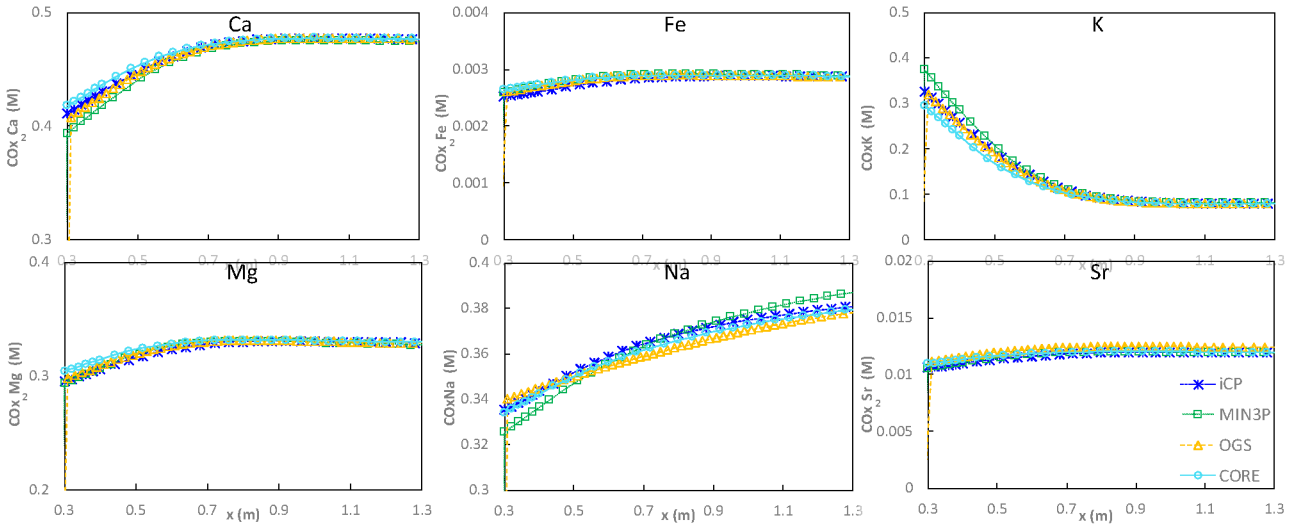

Fig. 15. *Cation concentration (M) profiles in COx exchanger at 1,000 years obtained with iCP, MIN3P, OGS-GEM and CORE^{2D}.*

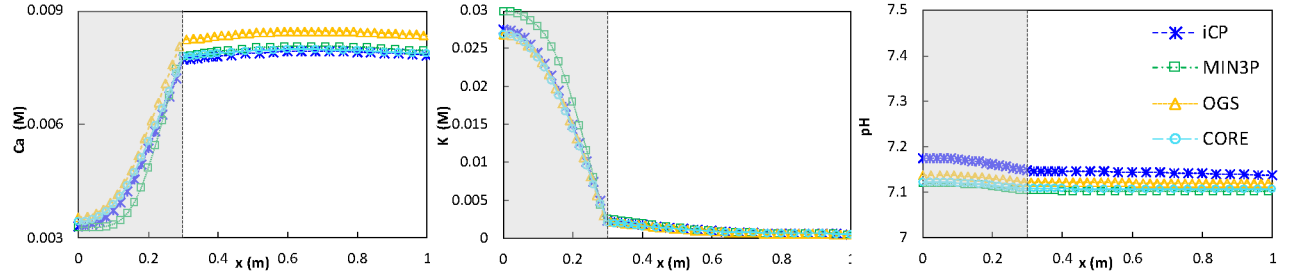

Fig. 16. *Total aqueous concentrations (M) and pH profiles at 1,000 years obtained with iCP, MIN3P, OGS-GEM and CORE^{2D}.*

7.2.3 P3: Minerals in equilibrium

The setup of case P3 is equivalent to the FRC but without accounting for the kinetically-controlled minerals. The only exception is quartz, which is included in case P3 as secondary phase in thermodynamic equilibrium in both materials, although in the FRC it was considered as a kinetically-controlled mineral. Quartz is expected to form in the model when the C-S-H gel dissolves. This case was simulated with iCP, MIN3P and CORE^{2D}. It is to note that in MIN3P, mineral reactions can only be simulated using kinetic rates. Thus, fast kinetic rates ($1 \cdot 10^{-9}$ mol/L_{medium}/s) were considered for all minerals to mimic thermodynamic equilibrium conditions. The results after 100,000 years are presented in terms of pH and porosity (Fig. 17) and mineral profiles (Fig. 18 and Fig. 19). The results of CORE^{2D} are the same as those included in the FRC comparison.

Overall, a very good agreement is observed between the results obtained with the different codes, with very small differences in pH and porosity profiles. However, the sensitivity of the system to iron is noticeable in the magnetite and siderite profiles.

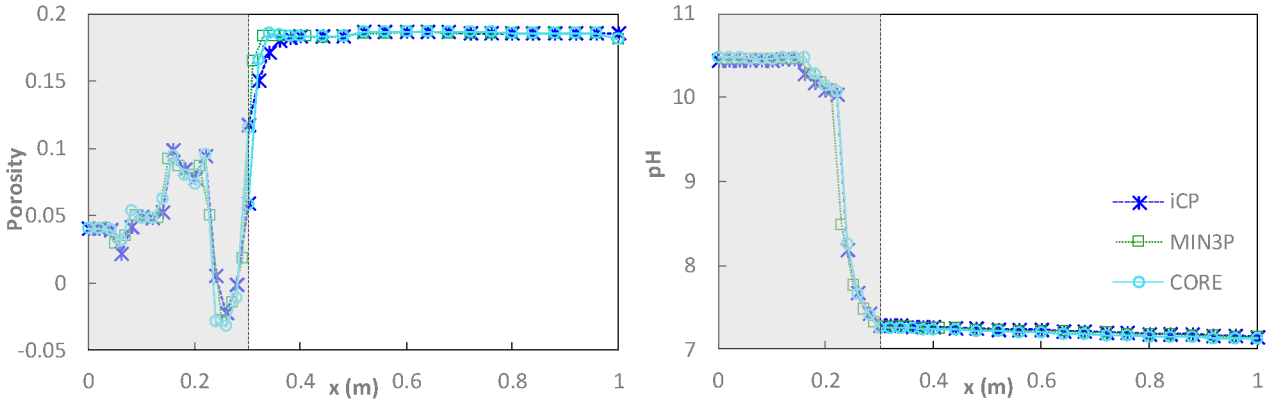

Fig. 17. *Porosity and pH distribution profiles at 100,000 years obtained with iCP, MIN3P and CORE^{2D}.*

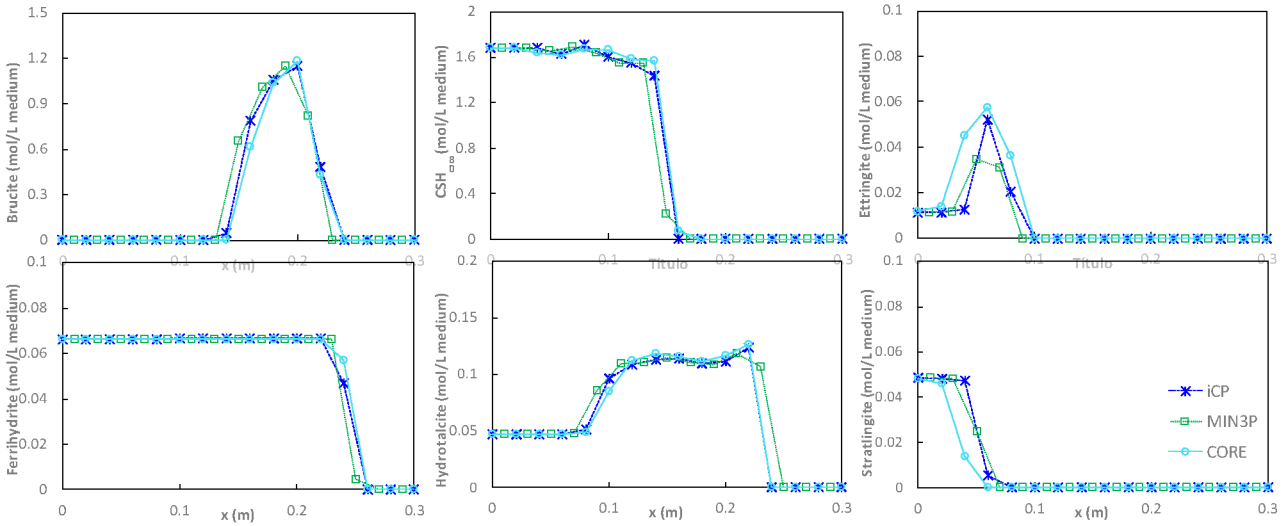

Fig. 18. *Mineral phase profiles (in mol/ L medium) in the concrete domain at 100,000 years, obtained with iCP, MIN3P and CORE^{2D}.*

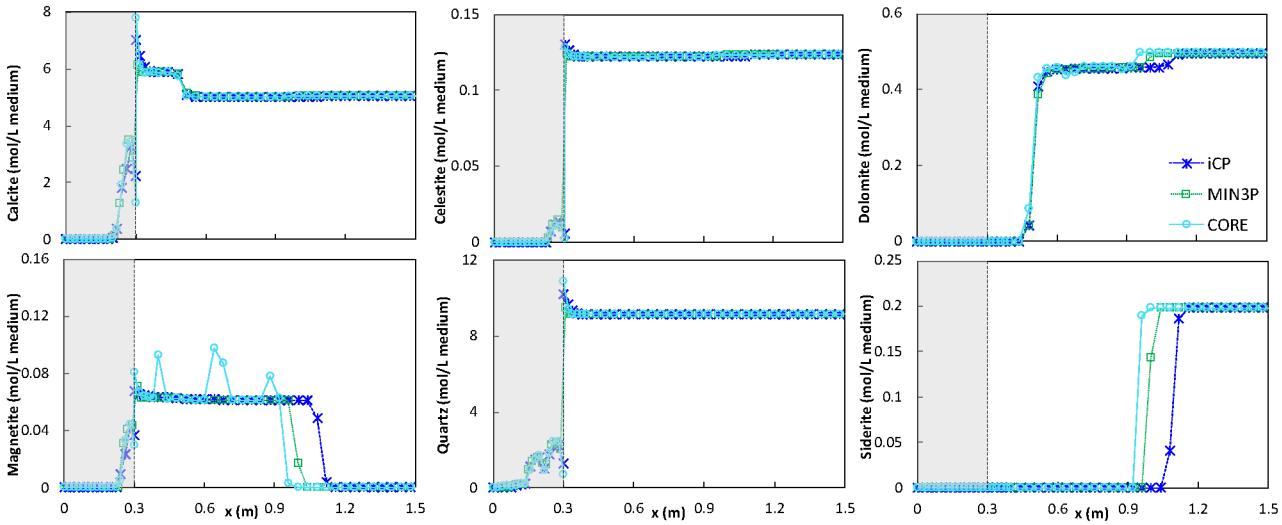

Fig. 19. *Mineral phase profiles (in mol/ L medium) in concrete and clay domains at 100,000 years, obtained with iCP, MIN3P and CORE^{2D}.*